Universidade do Minho
Escola de Engenharia

Helder Filipe Vilaça Faria

Evaluation of the thermoelectric properties of transparent Sb-doped zinc oxide thin films

January 2023

Evaluation of the thermoelectric properties of transparent Sb-doped zinc oxide thin films

Helder Faria

UMinho | 2023

Universidade do Minho
Escola de Engenharia

Helder Filipe Vilaça Faria

Evaluation of the thermoelectric properties of transparent Sb-doped zinc oxide thin films

Master Thesis
Integrated Master in Physics Engineering
Devices, Microsystems and Nanotechnologies

Thesis performed under supervision of
Carlos José Macedo Tavares

January 2023

COPYRIGHT

AKNOWLEDGEMENTS

The composition of this thesis was a rewarding final mark of my degree and master's in Physics Engineering, whose arduous steps, such as this one, made it so much more gratifying. It was five years of scientific exploration which proportioned me with a great deal of knowledge and most of all personal growth. With this came so many memories that I will cherish for the rest of my life, and the most important takeaway that I have are the people that followed me, but most importantly pushed me through this stage of my life, with unconditional support and motivation that made every challenge easy to overcome. It's something that I will never be able to repay, but at the minimum, I must leave a mention.

First and foremost, I would like to thank my supervisor Dr. Carlos Tavares for guiding me through this work, giving me the tools necessary to do it, and for his readiness and availability to always indulge me, my questions, and difficulties. I cannot go without thanking my colleague Joana Ribeiro too, which also served as a supervisor without having to. I'd like to thank her for all the patience and time she took to teach me and show me how the techniques and processes work, and mostly for putting up with my mindless errors and questions.

Finally, I would like to thank my family and friends. To my parents Noémia and António for letting me find my way and always supporting my choices, allowing me to do something I love, and to my sister Eva for all the love and emotional support that made the completion of this degree possible. Last but not least, I would like to thank my long-time friends for remaining by my side in this journey and the friends that university gave me for making these the best years of my life. I'd love to thank my friend Carlos Gil in particular, for being my partner in crime and dragging me to endless nights of studying that ultimately made it possible to reach this final stage and complete my objectives.

STATEMENT OF INTEGRITY

I hereby declare having conducted this academic work with integrity. I confirm that I have not used plagiarism or any form of undue use of information or falsification of results along the process leading to its elaboration.

I further declare that I have fully acknowledged the Code of Ethical Conduct of the University of Minho.

ABSTRACT

Evaluation of the thermoelectric properties of transparent Sb-doped zinc oxide thin films

Global energy demand has significantly increased in the past decade, to a point that modern technologies might not keep up, and the search for clean energy also takes part in making the development of proper solutions difficult. Wasted heat recovery systems have become popular due to the large opportunity for this technology associated with the tremendous loss in energy through the form of heat. Several new ways of heat harvesting are being developed, but thermoelectric technology has gained significant relevance. The advancements in thermoelectric materials and devices have paved the way for new strategies in heat harvesting systems. Transparent conducting oxides have gained popularity in thermoelectric technology as they can transport electricity while being optically transparent. Furthermore, transparent oxides can have thermoelectric properties, as is the example of ZnO, but tend to be limited by their inherent properties. ZnO does not have the conducting properties necessary for this type of application, but studies focused on the doping of this material have shown that those properties can be enhanced.

This study focuses on understanding the influence of Sb-doping in the ZnO electrical, optical and thermoelectrical properties, with the addition of also studying its structural and morphological parameters. For that, several samples with different doping levels were produced through magnetron sputtering and their respective important properties were measured in several analyses. As a result, thin ZnO:Sb films with an average transparency greater than 80% were produced, with an absolute Seebeck coefficient of 100 μV/K and respective Power Factor of 1.1 $mW \cdot m^{-1} \cdot K^{-2}$, effectively modifying the electrical, optical and thermoelectrical properties of the material and ensuring its suitability for thermoelectric applications.

Keywords: Antimony; Seebeck Coefficient; Thermoelectric; Thin films; ZnO.

RESUMO

Estudo das propriedades termoelétricas de filmes finos transparentes de óxido de zinco dopado com Sb.

A procura global de energia aumentou significativamente na última década, de tal forma que as tecnologias modernas podem não acompanhar, e a procura de energia limpa também contribui para tornar difícil o desenvolvimento de soluções adequadas. Os sistemas de recuperação de calor desperdiçado tornaram-se populares devido à grande oportunidade para esta tecnologia associada à tremenda perda de energia através de calor. Várias novas formas de captar calor estão a ser desenvolvidas, mas a tecnologia termoelétrica ganhou relevância de forma significativa. Os avanços nos materiais e dispositivos termoelétricos abriram o caminho para novas estratégias nos sistemas de captação de calor. Os óxidos condutores transparentes ganharam popularidade na tecnologia termoelétrica, uma vez que podem transportar eletricidade mantendo-se opticamente transparentes. Além disso, os óxidos transparentes podem ter propriedades termoelétricas, como é o exemplo do ZnO, mas tendem a ser limitados pelas suas propriedades inerentes. O ZnO não tem as propriedades condutoras necessárias para este tipo de aplicação, mas estudos focados na dopagem deste material têm demonstrado que essas propriedades podem ser melhoradas.

Este estudo centra-se na compreensão da influência da Sb-doping nas propriedades elétricas, óticas e termelétricas do ZnO, e de também estudar os seus parâmetros estruturais e morfológicos. Para tal, foram produzidas várias amostras com diferentes níveis de dopagem através de pulverização magnética e as suas respetivas propriedades importantes foram medidas em várias análises. Como resultado, foram produzidos filmes finos com transparência superior a 80%, e um coeficiente Seebeck absoluto de 100 μV/K e o respetivo Fator de Potência de $1.1 mW \cdot m^{-1} \cdot K^{-2}$ foram alcançados, modificando efetivamente as propriedades elétricas, óticas e termoelétricas do material e assegurando a sua adequação às aplicações termoelétricas.

Palavras chave: Antimónio; Coeficiente de Seebeck; Filmes finos; Termoelétrico; ZnO.

INDEX

LIST OF ABBREVIATIONS

2D	Two Dimensional
Al	Aluminium
Al_2O_3	Aluminium Oxide
ALD	Atomic Layer Deposition
Ag	Silver
Ar	Argon
As	Arsenic
AZO	Aluminium-doped Zinc Oxide
Bi	Bismuth
Bi_2Te_3	Bismuth Telluride
BTC	Benzene Tricarboxylate
Cl	Chlorine
CNT	Carbon Nanotube
CSA	Camphorsulfonic Acid
CO_2	Carbon Dioxide
Cu	Copper
Cu_2Se	Copper Selenide
CuI	Copper Iodide
CVD	Chemical Vapor Deposition
DC	Direct Current
DMSO	Dimethyl Sulfoxide
EDX	Energy-dispersive X-ray Spectroscopy
$EMIMBF_4$	1-ethyl-3-methylimidazolium tetrafluoroborate
$FeCl_3$	Iron(III) Chloride
Ga	Gallium
GaN	Gallium Nitride
Ge	Germanium
GZO	Gallium-doped Zinc Oxide
HRSG	Heat Recovery Steam Generator
I	Iodine
In	Indium
ITO	Tin-doped Indium Oxide
IZO	Indium-doped Zinc Oxide
K	Potassium
Li	Lithium
MBE	Molecular Beam Epitaxy
Mg	Magnesium
$MoCl_5$	Molybdenum(III) Chloride
MOCVD	Metalorganic Chemical Vapour Deposition
MOF	Metal-Organic Framework
MWCNT	Multi-walled Carbon Nanotubes
N	Nitrogen
Na	Sodium
$NbCl_5$	Niobium(III) Chloride
O	Oxygen
P	Phosphorus
Pb	Lead
PbTe	Lead Telluride

PE	Piezoelectric
PEDOT	Poly(3,4-ethylenedioxythiophene)
PEDOT:PS S	Poly(3,4-ethylenedioxythiophene)-poly(styrenesulfonate)
PEPG	Piezoelectric Power Generation
PF	Power Factor
PLD	Pulsed Laser Deposition
PPy	Polypyrrole
QD	Quantum Dot
QDSP	Quantum Dot Superlattices
S	Seebeck Coefficient
Sb	Antimony
Sb_2Te_3	Antimony Telluride
SEM	Scanning Electron Microscopy
Si	Silicon
SiGe	Silicon-Germanium
SWCNT	Single-walled Carbon Nanotubes
SZO	Antimony-doped Zinc Oxide
TCNQ	Tetracyanoquinodimethane
TCO	Transparent Conducting Oxide
TE	Thermoelectric
TEC	Thermionic Energy Converter
TiO_2	Titanium dioxide
TPV	Thermos-Photo-Voltaic
Vis	Visible Range
WHR	Wasted Heat Recovery
XRD	X-ray Diffraction
Zn	Zinc
ZnO	Zinc Oxide
$ZrCl_4$	Zirconium(IV) Chloride
ZT	Figure of Merit

LIST OF FIGURES

LIST OF TABLES

1. INTRODUCTION

Energy is and will continue to be a crucial part of the everyday life of our society. With the increasing growth of the human population and its technological advancements, the demand for more energy grows coupled with humanity's evolution. Alongside the necessity for more and more energy, grows the demand for a clean way to produce it. It's crucial for new developments to search for environmentally friendly solutions, both to replace and to improve current technologies, but also to preserve the planet at the same time.

According to the Annual Energy Outlook 2021 made by the EIA [1], by 2050, global energy use is expected to increase nearly 50% compared to 2020, mostly caused by economic and population growth in countries that are on developing stages of their economy. These countries' rapid growth pressures a big increase in technology usage, transportation necessities and other means to boost their economy, which are demanding on energy consumption. Furthermore, developed countries also contribute to this increase with higher levels of electricity usage, for instance, in construction, appliances and lighting. Even though developed countries grant more clean energy solutions, when compared to their less developed counterparts, these are still not enough to keep up with demand.

Similarly, the World Energy Outlook 2021 [2] found evidence supporting the energy demand growth and its effect on carbon emissions. According to this study, the two-third energy-related carbon dioxide (CO_2) emission decline caused by the global pandemic in 2020 was quickly on track to rise in 2021 as a reflection of the global situation returning to normal and energy demand also normalizing as production and consumption return to standard levels, which, simply put, means that the effects of the global pandemic, which caused energy consumption and CO_2 emission to decline, are rapidly being reverted and coming back to the standard growth they had before the pandemic. Beyond transportation and production, electricity is a key factor in energy demand and consumption. As more technologies become a part of everyday life, more electricity is needed to accommodate buildings, lighting, air-conditioning, and other apparatus. This effect is so prevalent that in 2020 electricity was responsible for 36% of all energy-related CO_2 emissions. Furthermore, in the past decade, the level of emissions rose about 9%, associated with a rise in electricity demand of 25%, according to the study. This also reflects positive aspects of the evolution of renewable energy that prevented the rise of emissions to be as drastic as the

rise in demand. Nevertheless, it all comes together as motivation to implement and improve solutions for clean energy as demand does not show any signs of slowing down, possibly reaching an 80% increase in electricity demand by 2050.

Even though changes and new developments are taking place, the demand for energy, and in particular electricity, motivate an imperative search for new solutions, with the ultimate goal of being able to fuel the world with zero emissions. Of course, this objective is far from reachable at the current stage, but every step toward its accomplishment is crucial. Therefore, renewable energy and its increase in efficiency is the main focus of present strategies. Wind and solar-related systems are the most efficient current solutions, but other technologies begin to show some promise.

2. HEAT

With the growing concern for avoiding the exhaustion of the earth's resources as well as the rising threat regarding global warming and the impact of technology on the environment, engineering industries are challenged with the task of reducing greenhouse gas emissions, while at the same time improving the efficiency of their systems to cope with the increasing global demand. There are several renewable sources of energy, such as water, wind, or solar, and their employment in today's global energy production has been significant. But, as previously mentioned, these technologies still need time to become a primary source of energy. Therefore, they have been stepping out of the spotlight of promising energy sources because of their current limitations. Consequently, heat has become a prominent subject in this area. Researchers have always been aware that heat is everywhere, and it represents a big slice of potential energy not being used, and as technologies advance heat promises to be a valid solution.

The focus of heat-related technologies lies in wasted heat. Wasted heat is the energy that is generated in any given process which is not put to any practical use and is lost, wasted, and dumped into the environment [3]. This type of waste is so prevalent that a study conducted by [4] found that 41% of global primary energy consumption is energy in the form of heat, but only 5% is useful in appliances such as heaters and burners. About 36% of the energy produced is lost in heat transfer processes, therefore more than a third of the global energy produced is wasted heat. With such potential for energy saving in today's big industrial environments, Wasted Heat Recovery (WHR) systems have become an important part of industrial processes, being one of the major areas of research to reduce fuel consumption, improve efficiency and lower harmful emissions.

2.1 Wasted Heat Recovery Systems

WHR is a group of systems and technologies that reutilize wasted heat. They are typically used in industrial environments because, there, the amount of heat produced and dissipated is larger. On top of that, some systems focus on redistributing this heat or even reutilizing it in the machine that produced it.

In a nutshell, they compose all the technologies that focus on making efficient systems that have none or minimal heat loss. Powered by the interest in new energy-related systems previously mentioned,

WHR has gained significance over the last decade with the development of new devices and technologies aiming to reduce wasted energy.

2.1.1 Heat transport and recovery

There are several types of WHR systems with different functions and different types of operation, but the most common are burners. These structures can be regenerative and recuperative, and they optimise energy efficiency by incorporating heat exchanger surfaces to capture and use the waste heat from the hot flue gas from the combustion process [3]. More simply put, these systems use the wasted gas produced in the combustion to heat the machine and keep the combustion going. They are typically used in large industries, but this technology is also employed in commercial appliances and shows gains in efficiency.

Economisers are other WHR systems which are mainly used for heating liquids and are commonly used in daily apparatus. The system consists of tubes, which the liquid passes through, covered by metallic fins to maximise the surface area of heat absorption and heat transfer rate. The device lets the liquid travel within these finned tubes perpendicularly to the flow of exiting gas allowing it to absorb the heat, transferring heat from the flue gases into the water flow and increasing efficiency by reutilizing the heat that would be lost in the exiting exhaustion [5].

Waste heat boilers are similar systems in the way that they use several water tubes that are placed parallel to each other and in the direction of the heat leaving the system aiming to generate heat as output, which is then used for power generation or directed back to the system for energy recovery [3].

Comparably to heat boilers, air preheaters work by the same principles but are designed to heat air before another process, increasing efficiency. There are different types of air preheaters that vary in the configuration: regenerative preheaters, where heat is transferred from the flue gases to a solid matrix which is then cooled by the combustion air, thereby preheating the air; rotary regenerators, which work the same way but with a rotative device functioning as the heating matrix; and recuperative preheaters, which reutilize the flue gases as the combustion air, resulting in the return of energy in the system reducing the amount of energy that has to be supplied [6].

Plate heat exchangers are used to transfer heat from one fluid to another. These systems consist of a pack of corrugated metal plates with portholes for the passage of the two fluids between which the heat transfer will take place. These plates are packs typically assembled between a fixed frame plate and a movable one, and the number of plates is determined by the flow rate, physical properties of the fluids

and working pressures and temperatures desired. The objective of this setup tends to be heating one fluid using the other, generally to refuel the system where it's being used creating a cycle [7].

Heat pipe systems are highly effective passive devices used to transfer heat at high rates over considerable distances with extremely small temperature drops, have exceptional flexibility, are simple to construct, and are easy to control, not needing external pumping power. Their configuration consists of a sealed container, a wick structure and a working fluid that is in equilibrium with its own vapour [8]. In a nutshell, when heat to applied in one end of the pipe, it is conducted along the wall and wick and evaporates the working fluid. As result, a vapour pressure is created which drives the vapour to the other end of the pipe. There, the vapour condensates, transferring the heat to its destination, and the fluid cycles back to the origin of the pipe to be repurposed. On the other hand, heat pumps are a type of system that serves the same purpose as a heat pipe, but they typically collect heat from air, water, or soil, and because of their simplicity they are often utilized in domestic settings. They are generally used to heat air or water and are most employed as alternatives to furnaces or air-conditioning, proving to be an efficient solution even though they need electricity to function [9].

All these systems can, of course, be implemented together depending on the desired application. A good and common example is the heat recovery steam generator (HSRG). This system's most common application is in a combined-cycle power station, where the hot exhaust gas produced from a gas turbine is fed to an HRSG to produce steam to drive a steam turbine [10]. The system can additionally recover the wasted heat from the exhaust. As previously said, the HSRG is a combination of several heat recovery systems, for example, an Evaporator, Super heater, Economizer, and Drum. This is but an example of a mix of some of the existing heat-recovering systems as there are many more.

Once again, there are many other systems and combinations of systems designed to harvest wasted heat and turn it into usable energy, but most, if not all of these examples are typically employed in an industrial environment because, in order to achieve efficiency levels that justify the investment in this technology, there needs to be a big quantity of heat flux in the system.

2.1.2 Direct electrical conversion

Some systems that are designed to produce electricity directly from wasted heat, not requiring converting heat into mechanical energy in between. The most common examples are thermoelectric (TE),

piezoelectric (PE), thermionic and thermos-photo-voltaic (TPV) devices and phenomena designed for electricity generation.

2.1.2.1 Piezoelectric power generation

The piezoelectric effect is the production of electric charge generated in certain materials in response to mechanical stress applied. This phenomenon is widely used in many fields because of its versatility. Mechanical stress can be induced in several ways, and its presence is typically a side effect of a natural action taking place, from wind blowing into a rod on top of a building causing it to shake, to a person pressuring the ground just by running or walking. Therefore, this effect and materials can and are used in several daily-basis energy-harvesting contexts, such as fluid-structure interaction, human movement, vibration and many more [11].

Piezoelectric Power Generation (PEPG) is the process of converting low-temperature heat energy directly to electricity. Typically, these heat recovery systems are constituted by a simple cantilever setup, which tends to be a simple but efficient solution. Assembled with thin-film membranes made with piezoelectric materials, these setups are applied in gas exhaustion systems, where heat causes oscillatory gas expansion. These vibrations are then turned into electricity that powers the apparatus where the structure resides or other systems nearby, effectively transforming the mechanical energy caused by wasted heat into usable electricity [12,13]. Even though these systems sound promising, PEPG technology comes with many technical challenges associated, such as low conversion efficiency, high internal impedance, the requirement for oscillatory heat loads and electrical signals, complex oscillatory fluid dynamics within the liquid/vapour chamber, and difficulty achieving long-term reliability and durability [14]. But the main issue associated with these systems is their very high cost. PEPG devices need high power generation capacity to achieve economic efficiency, high reliability for low maintenance cost, and high stability for easy control and wide application, becoming systems with a high cost of manufacturing [15].

2.1.2.2 Thermionic generators

A thermionic generator, or thermionic energy converter (TEC), is essentially a diode valve in which electrons from a hot cathode flow to a cooler anode, producing an electric current which can be used in an external circuit, with, usually, a gas or vapour introduced to provide ions to neutralize the space-charge of the electrons [16].

In its basic form, a TEC consists of two electrodes, a hot cathode (Emitter), which is heated to a sufficiently high temperature to emit high-energy electrons, and a cooler anode (Collector), which receives the emitted electrons and is operated at a significantly lower temperature. They are separated from one another by an interelectrode gap, which can be comprised of vacuum, vapour, or plasma. Furthermore, there's also an electrical load and an electrical connection. As the trapped electrons on the surface of the Emitter gain kinetic energy via the heating of said material, they overcome the energy barrier that keeps them trapped and escape the surface. These electrons then travel through the interelectrode space and are collected into the colder Collector. When a negative charge is accumulated, the electrical connection between the two electrodes creates a voltage difference that will drive a current through the electrical load, generating electricity. The electrons finally return to the Emitter and the cycle continues [17].

The application of these systems, however, shows to be limited. TEC devices need high temperatures (above 1200 K) to become efficient, lowering the number of devices where this technology can be used drastically. More so, the capability of this technology is still in development, but it shows promise, even in solid-state thermionics, where new advances are being made as materials are improved and become more efficient without creating additional pollution [18].

2.1.2.3 Thermo-photo-voltaic generators

A TPV generator is a system capable of converting the radiant energy emitted by an artificial heat source, for instance, the combustion of a fuel, into usable electrical energy via photovoltaic cells. These devices are comparable to solar panels, but use wasted heat as fuel for energy production [19].

A TPV generator consists of a pre-heating system, utilizing combustion to produce a fuel gas, working as the heat source, that will power a three-part array of an emitter, a filter, and photovoltaic cells. The emitter, when heated by the heat source, emits electromagnetic radiation. The filter ensures that only the radiation waves with the correct wavelength matching the photovoltaic cells pass through and, finally, the cells convert the radiation to electrical energy [20]

TPV generators tend to find good efficiency ratios on energy conversion but are limited by operating temperature range, where the increase in temperature decreases their efficiency [21]. Nevertheless, these devices are common and a good solution for large combustion and high efficiency photovoltaic cells that can withstand high temperatures exist, however, they are expensive. Therefore, one of the main focuses in TPV technology development is to reduce cost-efficiency levels [22].

2.1.2.4 Thermoelectric generators

TE generators have gained significant interest in the past decade as developments increase efficiency and make this technology viable. In short, the TE effect is the conversion of temperature differences in electric voltage and vice versa. When a TE material is subjected to different temperatures, creating a temperature gradient, it generates a current. Conversely, when these materials are subjected to different voltages, they generate heat. Therefore, an obvious use for these types of material is WHR, but their significance was always overlapped by the difficulty of creating an efficient system that could compete with other types of technologies, both in price and capability. These systems have already shown a wide range of relevant applications such as automotive, engines, industrial exhaust systems and even glass or metal furnaces [23,24]. Nevertheless, even though this technology shows great promise, and keeps improving, it still has issues and challenges at present, mostly around heat transfer rates and, more importantly, viable materials.

Nonetheless, an opportunity for enhancement arises as new materials are studied, and new setups are created. From here comes the main focus of this thesis: the study of materials to utilize and improve electrical generation with TE technology.

2.2 Thermoelectric effect

As previously mentioned, TE-based technology has had a positive impact on modern recovery systems. It bases itself on the harvest of energy in the form of heat which would otherwise be lost. Systems like this have ensured that it is possible to use this, once thought, unusable energy. Thermoelectricity, as the name implies, is a phenomenon in which thermal energy, or heat, can be directly converted into electricity. This capability, acknowledging that thermal waste takes a large portion of all wasted energy, is, clearly, very appealing, but it has been paid small attention to because of the absence of ways to apply it efficiently. Probably, the biggest example is the struggle with the choice of materials. Not all materials have TE characteristics, and the few studied ones tend to have their specific problems, whether it is price or scarcity, toxicity or even sometimes challenges in efficient application. Therefore, it's imperative to explore more possible TE materials to work in parallel with the new developments made in this area. Going into more detail, the TE effect is the direct conversion of temperature differences to electric voltage and vice versa via a thermocouple. More simply put, a TE material creates a voltage when it is submitted to different temperatures on each side, and conversely, the opposite happens when a voltage difference is applied.

2.3 Thermoelectric materials

Necessarily, TE materials must be able to conduct electricity and heat, therefore they typically fall in the categories of conductors and semiconductors, and, because the intrinsic properties of most materials display less advantageous values of conductivities, most of the time, the used materials are compounds such as alloys and complex crystals. By creating complex bulk materials and creating layered structures, it's possible to maximize the efficiency of materials and devices.

The objective of enhancing the efficiency in TE materials, whether by doping or combining said materials, is to increase the electrical conductivity and the Seebeck coefficient, and, at the same time, lower the thermal conductivity, maximizing the figure of merit (ZT). Although there is no known theoretical limit to ZT, in practice it has been difficult to achieve high ZT values because of the inherent coupling of electrical conductivity and thermal conductivity in most materials [14]. Nonetheless, the most commonly used materials tend to achieve ZT lower or equal to 1 in their primary form but can be enhanced.

2.3.1 Thermoelectric materials with common applications

Certain materials have had the spotlight as good TE materials for some decades. A good example is bismuth telluride (Bi_2Te_3), which is one of the best-performing room-temperature TE materials with a temperature-independent ZT, between 0.8 and 1.0 [25]. They have been used extensively in TE refrigeration applications and some niche low-power generation applications, and have a useful temperature range of 180 to 450 K. Furthermore, nanostructuring this material to produce a layered superlattice structure of alternating Bi_2Te_3 and antimony telluride (Sb_2Te_3) layers results in a device with good electrical conductivity, but poor thermal conductivity, with enhanced ZT of approximately 2.4 at 300 K for p-type [26]. Many other variations of Bi_2Te_3 have shown high ZT and are commonly used in room temperature applications, namely refrigeration, but these compounds tend to be limited by the toxicity and rarity of tellurium.

Another ordinarily used TE material is lead telluride (PbTe), which showed a ZT value of 1.5 at 773 K [27] when doped with thallium and 1.4 at 750 K with sodium (Na) doping [28]. Additionally, a ZT of 1.8 was demonstrated in Na-doped $PbTe_{1-x}Se_x$ alloy [29]. Many more combinations of PbTe have been studied and these materials have been used extensively in higher temperature power generation applications, particularly spacecraft power generation, having a useful temperature range of 500 to 900 K, typically.

An interesting material, and target of great focus in many areas, is silicon (Si). Si finds its way into thermoelectricity too, even though bulk Si shows ZT values of 0.01. It reveals promising results when combined and configurated in specific ways. For instance, it can reach values of 0.6 for ZT when turned into nanowires. Moreover, Si is commonly combined with germanium (Ge) improving ZT values, being the current best TE material around 1300 K, but limited by the high price and still moderate values of efficiency. Nonetheless, its ZT can be increased to 1-2 with SiGe nanostructures, greatly owed to the reduction in thermal conductivity [30].

Other significant examples are compounds of magnesium (Mg) and group-14 elements, such as $Mg_2Si_{0.55-x}Sn_{0.4}Ge_{0.05}Bi_x$ which showed ZT values of 1.4 at 800 K [31], or Skutterudites, which combine rare-earth materials to reduce thermal conductivity by producing sources for lattice phonon scattering, without reducing electrical conductivity, and have shown ZT values of 1.0 or higher [32].

Among these, many other types of compounds and materials are relevant to TE applications and find their way into refrigeration and power generation devices within all temperature ranges.

2.3.2 Transparent Conducting Oxides

Among TE technology we find transparent conducting oxides (TCOs), which are electrically conductive materials with high transparency in the visible range. TCOs have been investigated for a wide range of applications in optoelectrical devices including photovoltaics, displays, transparent electrodes in touch panels, optoelectrical interfaces and window glass technologies [33,34]. They represent a good solution in the field of thermodynamics and energy production, more and more due to the advancements in transparent technology propelled by the growing demand for devices like phones, tablets, TVs, and so on, that, more than ever, are basic utilities for the consumer. Just like most other TE-based devices, when TCOs are applied they harvest wasted energy passively, connecting to an apparatus or network and collecting the energy that would've been wasted without affecting the normal functionality of the system. Practical daily examples of possible ways to implement such technology are easy to come up with. For instance, applying a TCO layer on the screen of a cell phone or TV, any device with a screen or display, would give the possibility of harvesting energy to power that same device by the natural temperature difference between the inside and outside of said device. Another passive and promising way of utilizing TCOs would be to apply them in skyscrapers or building windows, where, typically, the sun would heat the external part of the glass, which would oppose the colder interior, standard to daily working environments. However, as good or revolutionary as these ideas, and many others, may seem, there is

still a lot of work to be done to make these materials and technology viable for these types of applications. Materials need to be studied and optimized, and geometry and devices for their usage must be developed to justify the investment.

The most utilized TCO is tin-doped indium oxide (ITO) [35], being commonly used because it is easy to fabricate and possesses good conductive properties, essential for its application. However, it's difficult to access because of the scarcity of attainable indium (In). Furthermore, its poor chemical stability in hydrogen atmosphere and high toxicity create a great interest in the development of new alternative TCOs. *IDTechEx* research forecasts that transparent conductive films alternative to ITO will reach a combined market value of $220 million and new market opportunities will represent nearly 45% of the total TCO market in 2027 [36]. On the other hand, the market for TE energy harvesters is estimated to reach over $1.5 billion by 2028 [37] so the already growing interest in TCOs is justified by this new opportunity that presents itself. Associated with this is the fact that, even though TCOs are well understood and widely used commercially, and they have been tested for their TE capabilities, their performance is far below that needed for industrial deployment [38]. This shows a promising opportunity in developing a new solution in optically transparent conducting materials and gives grounds for this paper.

Concerning the proper creation of an implementable solution, it's necessary to improve certain characteristics of the TE materials, specifically a TCO. It has been shown that reducing the lattice thermal conductivity is vital for improving the TCO TE efficiency, as it was found to be the most variable parameter between the TCOs, making it a crucial factor in their ZT. This happens because of the very long phonon mean free paths, making them strong candidates for nanostructuring to increase performance [38]. Even though a wide range of TE materials have been studied and explored, some of which were previously mentioned, a high ZT value remains connected to bulk materials [39]. The problem is that, because of their small band gap, these types of materials tend to be optically opaque, not constituting a valid solution to the intended applications [40]. This opens the way for thin films based on TCO materials, which can be optimized to become a good solution for TE applications, having a high ZT without losing the transparent characteristics of the material.

2.3.3 Seebeck Effect

In 1821, Thomas Johann Seebeck, following experiments with voltaic current and magnetism, found that a circuit made from two dissimilar metals with junctions at different temperatures would deflect a compass magnet. He believed that this was due to magnetism induced by the temperature difference,

reasoned by the lack of knowledge of the electron at the time, so he elaborated a table relating different metal junctions and the deflexion of the compass. At the time, discussions about different beliefs arose with this experiment. Seebeck and others believed in the polarity of Nature, focusing on forces of Nature such as electricity, magnetism, heat, etc. Others pursued explanations based on Newton's concept of force. Ultimately, after the discovery of the electron and its fundamental charge, scientists concluded that Seebeck's effect was not a manifestation of magnetic properties, but an electric current induced by the temperature difference, which then deflected the magnet, following Ampere's law. So, this experiment became the "birthplace" of the TE effect.

Now we know that the Seebeck effect is the electromotive force that develops across two points of an electrically conducting material, conductor or semiconductor, when there is a temperature difference between them. To describe it there's the Seebeck coefficient which is the ratio between the electromotive force and the temperature difference.

$$S = -\frac{\Delta V}{\Delta T} \tag{1}$$

With ΔT being the difference between the temperatures applied on the edges of the material and ΔV representing the respective measured potential difference, the Seebeck Voltage [41]. This value is of extreme importance when characterizing a TE material.

To explain the atomic behaviour of this effect a simple setup just like the one in Figure 1 is enough. It is a TE generator, such as the ones describes in the previous chapters, and it is composed of two materials of different Seebeck coefficients, one p-doped, known as an acceptor because it is lacking in electrons, so it's positively charged, and one n-doped, known as a donor, which, inversely, has extra electrons than the original undoped material, creating a negative charge. Both these materials are connected to a heat source and a heat sink, creating a heat flux between them. This causes the charges to follow the direction of the heat transfer in both TE materials, generating a voltage along them, creating a current from the p-type material to the n-type material, and the magnitude of the voltage produced is proportional to the temperature gradient. On a quick side note, the other configuration in the picture is one to describe the Peltier effect, which is the inverse of the Seebeck effect, i.e., it is the generation of a temperature gradient between the junctions of two conducting materials caused by an applied voltage, and it has the same working principle, but does not deserve much explanation because it is not relevant for this study.

This simple setup shows the basic working principle of the Seebeck effect on which all TE systems are based. The physics behind the configuration are always the same, but the parts used to create it

dictate its efficiency. Apart from charges, cables, decent heat sources and sinks, and other basic elements depending on the desired application, the materials used in the structure will determine its capacity to convert heat into electricity. Therefore, these materials must have certain properties to be viable.

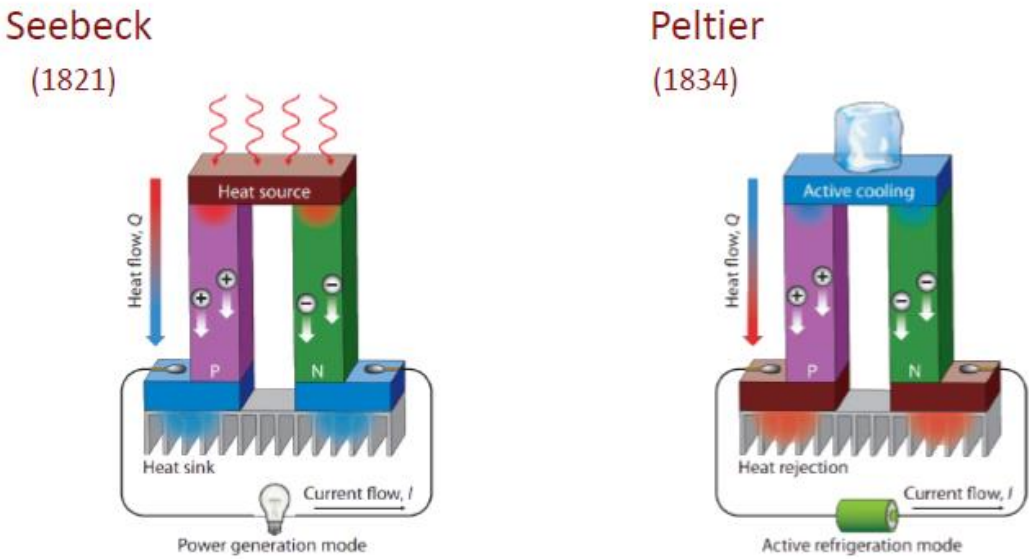

Figure 1: TE generators to exemplify the Seebeck and Peltier effect: Seebeck (left) and Peltier (right).

2.3.4 Important properties of thermoelectric materials

In order to have a good configuration in a TE generator, the following general characteristics are desirable in a good TE material [42]:

- High Seebeck coefficient, for maximum conversion of heat to electrical power;
- High electrical conductivity, to minimize Joule heating (Joule or resistive heating is the process by which the passage of an electric current through a conductor produces heat);
- Low thermal conductivity, to retain maximum heat for conversion at the hot junction and avoid losses down the limbs to the cold sink, preventing thermal conduction through the material.

All these characteristics are combined in the previously mentioned quantity denominated ZT, which equates all properties above and is given by:

$$ZT = \frac{S^2\sigma}{k}T \tag{2}$$

Where T is the operating temperature in Kelvin (K), S is the Seebeck coefficient (V/K), σ is the electrical conductivity ($\Omega^{-1}\cdot cm^{-1}$ or $S\cdot cm^{-1}$) and k is the thermal conductivity ($W\cdot m^{-1}\cdot K^{-1}$).

This important parameter dictates the magnitude of the maximum power conversion efficiency of performance for TE materials and devices [14].

An alternative type of comparative measurement for TE materials is the Power Factor (PF), usually measured in $W \cdot m^{-1} \cdot K^{-2}$:

$$PF = S^2\sigma \tag{3}$$

Which is a quantifier that does not use thermal conductivity in its calculation, typically used for comparisons and evaluations where the thermal conductivity can't be determined.

3. THERMOELECTRIC MATERIALS FOR THIN FILM TECHNOLOGY

Thin film technology has been implemented for over half a century and it has become an intrinsic part of everyday appliances, both domestic and industrial. They offer different ways of utilizing common materials, and they have opened several possibilities, both in industrial processes, such as in coatings for wear or corrosion protection, in energy-related systems, such as solar cells and panels, and even in day-to-day objects as in coatings for food storage. By applying materials in a thin layer, which can vary from nanometres to several centimetres, when several layers are applied, the materials showcase different properties, which often greatly differ from their bulk material form. Furthermore, it unlocks the way to combinations and intercalations of different materials. These different properties vary within the same materials as deposition conditions are altered, such as making a thicker or thinner film, or by changing environment characteristics such as temperature or ambient gases. For instance, by simply changing the film thickness it's possible to manipulate the optical properties of dielectric films to transmit or absorb specific wavelengths. This offers a wider spectrum of capabilities to all types of materials, giving a big focus of interest to this technology in recent years. Furthermore, certain thin films can retain features from their bulk form, such as electrical properties, but be optically transparent to visible light. This becomes particularly important when working with conducting materials, making TCO-based applications possible. Yet, thin film applications depend strongly on the electrical, optical, and physical properties of the materials chosen. These properties depend, in turn, strongly on the techniques and processes used to fabricate the films. As previously mentioned, surrounding conditions and settings directly affect the thin film and its properties. The same deposition tool and technique used, for example, to deposit a clear, dielectric film with excellent optical properties can, with small changes in the parameters, result in opaque, metallic films more suitable for electrical conduction than optical applications [43].

Such versatility finds its way into several fields of application. In the 1900s, when this technology was still in development, it was used in optical applications, such as mirrors for telescopes and then evolved to modern types of optical coating. It then gained relevance for their physical properties, such as

hardness and wear resistance, being used in instrument hard coatings and, further down the line, in microelectronics, for example in automobile parts, and even in normal day-to-day environments, such as windows in skyscrapers and as metal coatings present inside of bags of potato chips [43]. In more recent years, thin films have shown potential and have been widely studied for TE applications, making use of TE materials such as TCOs [44].

The range of materials used in thin film technology is limitless and there are examples of their application in all types of areas. Probably, the most commonly known are metals like copper (Cu), In and gallium (Ga) that, together with Si and other dielectric or ceramic materials, are used as semiconductors and other fundamental parts of electronics and microelectronics. Other metals, namely aluminium (Al), are applied as optical coatings to make mirrors. Still within the metal category, precious metals are more and more common in thin film applications. A big example is gold which is used in sensors and microarrays, or in biomedical applications, where films made of pure gold help to prevent contamination in sensitive cell cultures. Also, a lot of polymers are used as thin films, for instance, polyaniline are utilized in OLEDs for displays, and even oxides are ordinary materials in this technology, sometimes used in batteries or fuel cells [45]. Objectively, the examples of thin films being applied in modern technology are abundant, and, within these examples, there are also TE materials and applications.

3.1 Inorganic-based thin film thermoelectric materials

Inorganic TE materials found their way into thin film technology due to limitations in their bulk form, namely their low efficiency and high cost. Furthermore, recent studies found that the low-dimensional material design improves TE efficiency through more effective phonon scattering, contributing to a reduced lattice thermal conductivity, and, at the same time, increasing the PF [46]. Thin films and nanostructures have become popular due to this improvement, and this section will showcase common examples of fabricated thin films of typical inorganic TE materials and their performance.

3.1.1 Bi-Te-based thin films

Bismuth telluride and its solid solutions are good TE materials whose bulk forms are commonly used. They possess good TE characteristics, and, in recent years, their TE performance has increased by doping, more specifically, in thin film technology. In a study that carried out measurements with Bi_2Te_3 composites dispersed with silver (Ag) nanoparticles, the samples exhibited much lower thermal

conductivity and higher PF. A maximum ZT value of 0.77 at 475 K from the bulk Bi_2Te_3 dispersed with 2.0 vol% Ag nanoparticles, approximately three times higher than that of the Bi_2Te_3 matrix [47]. This increase in the bulk's form parameters goes to show how doping can affect the material's properties, and so the researchers found it to be a good study point. There are many examples of doping phenomena to be beneficial for the TE performance of several materials. A good example is bismuth telluride doped with lead (Pb) thin films, where the optimization of the carrier concentration significantly increased the Seebeck coefficient of the Bi_2Te_3 film and reduced the carrier thermal conductivity. For the as-deposited and annealed films doped with 0.38 at.% Pb, PFs of 2.50 and 2.15 $mW \cdot m^{-1} \cdot K^{-2}$ are achieved at 473 K, respectively [48]. Nonetheless, Bi_2Te_3 thin films are still useful when undoped. A recent study was able to develop flexible Bi_2Te_3 thin films using RF magnetron sputtering and achieving a maximum PF of 1.20 $mW \cdot m^{-1} \cdot K^{-2}$ [49]. However, even though Bi_2Te_3 is common in TE devices, other materials such as Zn and Cu and their thin film form have been studied recently due to their lower cost and higher abundance.

3.1.2 Cu-based thin films

Cu-based composites, both in bulk form and thin film, are of great interest to TE technology. Bulk copper selenide (Cu_2Se) has been reported to reach the highest ZT value of 2.4 at 1000 K when mixed with carbon nanotubes [50]. On the other hand, Cu_2Se thin films exhibit lower performance than that of their bulk form, but they have found relevance due to their flexibility. A flexible TE Cu_2Se thin film was fabricated by a low-cost and scalable spin coating process using ink solution and exhibited a PF of 0.62 $mW \cdot m^{-1} \cdot K^{-2}$ at 684 K on rigid aluminium oxide (Al_2O_3) substrate and 0.46 $mW \cdot m^{-1} \cdot K^{-2}$ at 664 K on flexible polyimide substrate, being among the highest values reported in all flexible TE films in recent years [51]. Furthermore, flexible and optically transparent copper iodide (CuI) thin films were assembled by reactive sputtering and achieved a ZT of 0.21 at 300 K, potentializing TCO technology [52].

3.1.3 Cobalt oxide-based thin films

There are several cobalt oxide composites, which largely vary in their formula, and there are many examples of their utility in TE technology. $NaCo_2O_4$ single crystal thin films showed a Seebeck coefficient of 100 $\mu V \cdot K^{-1}$ in the in-plane direction, and $Ca_3Co_4O_9$ was found and presented a satisfactory thermopower performance, with a Seebeck coefficient of 125 $\mu V \cdot K^{-1}$, with an electrical resistivity of 10 to 40 $m\Omega \cdot cm$, both at room temperature [53,54]. In more recent years, a flexible nanostructured $Ca_3Co_4O_9$ thin film was developed, showing a PF above 1 $mW \cdot m^{-1} \cdot K^{-2}$, and its flexibility made it bendable without any deterioration

of the TE performance [55]. When introducing nanoporous structures into $Ca_3Co_4O_9$ thin films, the TE performance improved due to the selectively scattering phonons, and this porosity can be controlled, determining the TE properties of the respective film. The lowest electrical resistivity found was around 7 mΩ·cm yielding a PF of 2.32 $mW \cdot m^{-1} \cdot K^{-2}$, near room temperature [56]. Furthermore, these films are transferable from the primary substrates to other arbitrary polymer platforms by simple dry transfer, which opens an opportunity for wearable applications.

3.1.4 Titanium oxide-based thin films

Titanium dioxide (TiO_2) is a material of particular interest and has been extensively investigated due to its optical and electronic properties and good stability in the adverse environment, which makes it a very versatile material [57,58]. Even though work has been done in improving this material's electrical conductivity, it is still necessary to reduce the thermal conductivity to effectively create a competitive TE material. Doping appears to be the best solution to ultimately reach a high ZT and PF, but the optical properties of the film are strongly dependent on the dopant. Recent studies in TiO_2 doped with niobium showed promising results as n-type films with a thickness of 120–300 nm and maximum average optical transmittance in the visible range of 73% reached a maximum TE PF of 60 $\mu W \cdot m^{-1} \cdot K^{-2}$ and ZT of 0.014, due to a reduced thermal conductivity of 1.5 $W \cdot m^{-1} \cdot K^{-1}$ [59]. In a similar study, niobium-doped reached a maximum PF and ZT of 0.5 $mW \cdot m^{-1} \cdot K^{-2}$ and 0.18 at a temperature of 300 K, respectively, for a 150 nm thick film, yielding a thermal conductivity of 1.3 $W \cdot m^{-1} \cdot K^{-1}$ [60]. The modifications to the optical, electric, thermal and TE properties of the thin films enable their suitability for applications as transparent electrodes in photovoltaic systems and touch displays, amongst other devices [59].

3.2 Organic-based thin film thermoelectric materials

Organic polymers inherently possess a low thermal conductivity, which gives them a significant advantage over conventional TE materials [61]. Additionally, they can be flexible and lightweight, contrary to other examples. Today's TE materials of choice for low-temperature energy conversion are bismuth antimony telluride alloys, elements that have a low natural abundance and some level of toxicity, making them expensive, which limits the widespread use of TE installations for waste heat recovery. This opened space for widely available, although less efficient, organic TE materials to become the subject of interest to the scientific community. These materials bring possibilities for mass production at low cost and are

solution-processable [62]. However, most polymers suffer from poor efficiency, requiring suitable doping agents to improve their TE performance. Therefore, numerous doped polymers have been researched for their TE properties and are commonly used, with the next section resuming some examples.

3.2.1 Polyacetylene-based thin films

Polyacetylene is a common organic polymer with high electrical conductivity but is unstable in the atmosphere, which is a fatal flaw in its application. Nonetheless, developments and studies with this polymer have been carried out and found that doping polyacetylene can increase its electrical conductivity, from 3×10^{3} $S\cdot cm^{-1}$ in un-doped polyacetylene to 10×10^{3} $S\cdot cm^{-1}$ in iodine-doped polyacetylene [63]. Other tested dopants, such as metal chlorides like iron(III) chloride ($FeCl_3$), molybdenum(III) chloride ($MoCl_5$), niobium(III) chloride ($NbCl_5$), and zirconium(IV) chloride ($ZrCl_4$), which were doped with polyacetylene and their properties were measured. As a result, the $FeCl_3$-doped polyacetylene film exhibited the highest value for electrical conductivity of approximately 30×10^{3} $S\cdot cm^{-1}$, which is still an increase compared to the previous example [64].

3.2.2 Polyaniline-based thin films

Polyaniline is a flexible well-known polymer that gain significance when its high electrical conductivity was verified. Furthermore, unlike polyacetylene, the electrically conducting emerald salt form of polyaniline is air-stable and can be produced on large scale at a low cost due to its easy synthesis and processing [65,66]. This polymer becomes interesting when doped with different elements, such as when combined with camphor sulfonic acid (CSA), where it showed good electrical conductivity between 10 and 300 K. The ideal doping level was 60% where the electrical conductivity reached its peak of 583 $S\cdot cm^{-1}$ [67]. Analogously to polyacetylene, polyaniline can't compete with inorganic TE materials when it comes to TE properties such as PF and thermal and electrical conductivity, but it can reach decent values and bring along advantages such as price, ease of production and flexibility.

3.2.3 Polypyrrole-based thin films

Polypyrrole (PPy) is a relevant polymer because it shows higher conductivity than the examples previously mentioned. In a series of PPy samples synthesized using different methods, using different dopants and relating different temperatures, the highest conductivity, 340 $S\cdot cm^{-1}$, was obtained for PPy doped with hexafluorophosphate [68]. In a more recent study, PPy films have been prepared by an

electrochemical method, and their TE properties were measured. The electrical conductivity peaked at 160 $S \cdot cm^{-1}$, but in that same instance, the Seebeck coefficient hit its lowest value of 6.7 $\mu V \cdot K^{-1}$, dropping from 51.0 $\mu V \cdot K^{-1}$, where the electrical conductivity was 15 $S \cdot cm^{-1}$ [69].

3.2.4 Polythiophene-based thin films

Polythiophene is yet another conducting polymer used in several electronic devices, such as diodes and biosensors. Polythiophene nanofilms showed to have decent TE capabilities, showcasing an electric conductivity of 47 $S \cdot cm^{-1}$, a Seebeck coefficient of 130 $\mu V \cdot K^{-1}$, and reaching a ZT of 0.029 at 250 K, higher than that of many other conducting polymers [70]. Although this does not surpass the TE capabilities of other types of materials, it gives grounds for a theoretical route of study for these types of polymers.

3.2.5 Poly(3,4-ethylenedioxythiophene)-based thin films

Poly(3,4-ethylenedioxythiophene) (PEDOT) also possesses conducting capabilities, but it has the added benefit of being optically transparent in its conducting state. In nanofilm form, it has shown electric conductivity of 73 $S \cdot cm^{-1}$ and a Seebeck coefficient of 76 $\mu V \cdot K^{-1}$, culminating in a ZT of 0.031 at 250 K, which is also higher than that of many other conducting polymers [70]. In a different study, poly(3,4-ethylenedioxythiophene) was combined with poly(styrenesulfonate) (PEDOT:PSS) and the TE properties were tuned utilizing two different methods, by adding dimethyl sulfoxide (DMSO) into the PEDOT:PSS solution, and with post-treatment of thin films with a mixture of DMSO and ionic liquid, 1-ethyl-3-methylimidazolium tetrafluoroborate ($EMIMBF_4$). The addition of DMSO to PEDOT:PSS solution improves the electrical conductivity with a concomitant minor reduction of the Seebeck coefficient. Nonetheless, the DMSO post-treatment shows to be more effective in improving the electrical conductivity with a trivial change in the Seebeck coefficient. The PF is increased up to 30.1 $mW \cdot m^{-1} \cdot K^{-2}$ for the film with DMSO posttreatment, while the optimized PF by DMSO addition is 18.2 $mW \cdot m^{-1} \cdot K^{-2}$. When $EMIMBF_4$ is applied, an optimized PF of 38.46 $mW \cdot m^{-1} \cdot K^{-2}$ is achieved, which is the highest reported so far for PEDOT:PSS thin films, with a corresponding ZT of 0.068 at 300 K. This demonstrates potential in post-treatment of PEDOT:PSS for the enhancement of its TE performance.

3.3 Inorganic-Organic based thin film thermoelectric materials

Conducting polymer thin films have great properties such as low density, low thermal conductivity, good electrical conductivity, and provide easy synthesis at a low cost, but they can't compete with inorganic TE materials due to their limitations in electrical conductivity and ZT value, therefore, it has not been feasible to apply these materials alongside TE generators. The combination of inorganic materials and organic polymers searches to take advantage of both benefits from these two types of materials and presents significant potential for producing relatively low-cost and high-performance TE materials [71].

3.3.1 Metal-Organic Frameworks

Metal-organic frameworks (MOFs) are a relatively new class of porous, crystalline materials with a broad range of applications. MOFs are composed of metal ions or clusters, which act as the joints, bound by multidirectional organic ligands, which act as linkers in the network structure. These networks go from one to three dimensions forming periodic structures. The joints and linkers assemble in such a way that regular arrays are formed resulting in robust, and often porous materials. MOFs are the highest reported surface area materials known, and most porous MOFs reported to date are microporous, therefore they have pore diameters of less than 2 nm, however, there have been a limited number of recent examples of demonstrated mesoporous MOFs, which means they can have pores with diameters reaching 50 nm. Besides much greater internal surface areas, MOFs offer significant advantages, when compared with materials of similar properties such as zeolites, in the prospect of predictable alteration of organic units to provide tailored materials for given applications. For example, the length of the organic linker often defines the size of the resulting pores of a given material. Furthermore, the functionalization of the organic unit can provide predictably functionalized pores [72]. Nevertheless, even though MOFs provide significant advantages, such as high surface area, high degree of porosity, intrinsically tunable chemical structure, flexible architecture, and multifunctional properties, the practical use of these novel materials has been restricted due to certain drawbacks including high fabrication costs, poor selectivity, low capacity, and difficulties in recycling/regeneration [73].

When it comes to TE applications, MOFs have been a point of interest since their electrical conductivity and potential for conductive opportunities have been reported [74]. A recent example of a successful conducting MOF was the composite of Cu with benzene tricarboxylate (BTC) of $Cu_3(BTC)_2$ and the guest molecule TCNQ (tetracyanoquinodimethane), which, when added, can increase the MOFs' electrical conductivity. That fact was verified and a Seebeck coefficient of 375 $\mu V \cdot K^{-1}$ at room temperature

was measured. This value is comparable to that of the best organic materials and exceeds that of bulk Bi_2Te_3, but even though the electrical conductivity increases with temperature it is still much lower than the conductivity of the materials referred before, therefore the TE properties of this composite are much lower than the best organic and inorganic materials [75]. Having said that, this still proves the potential of MOFs in energy-related technology. Other examples of conductive MOF materials are gradually emerging in many fields and exhibit outstanding performances, and although the field of electrical conductivity has not yet become the prime focus of research for MOFs, it has witnessed tremendous growth in the past ten years and various MOFs with high charge mobility and electrical conductivity have been successfully constructed [76].

3.3.2 Carbon Nanotubes

Simply put, carbon nanotubes (CNTs) are tubes made of carbon with diameters typically measured in nanometres. They can be divided into two categories: CNTs in which the wall structure consists of a single graphite sheet closed in a tubular shape are called single-walled carbon nanotubes (SWCNT), while those consisting of a plurality of graphite sheets each closed into a tubular shape and nested one within the other are called multi-walled carbon nanotubes (MWCNT) [77]. Like their building block graphene, CNTs' chemical bonds are strong, and when this cylindrical structure is formed, the nanotubes natural tendency to stick together, due to their Van der Waals forces, which provides the opportunity to develop ultra-high strength, low-weight materials that possess highly conductive electrical and thermal properties. With stiffness compared to diamonds and strength larger than steel, CNTs are commonly used in industrial and mechanical environments, but the added properties of very low weight and thermal and electrical properties make it a very interesting possibility for TE applications. They have gained significant interest mostly due to their remarkable electrical properties and low cost, and they have been used in many diverse implementations, such as enhancing the TE properties of TE material, for instance, organic materials like polyaniline [78,79], or in energy storage materials [80–82]. When it comes to thin film TE applications, CNT's electrical properties can achieve values that compete with some of the materials from this chapter. A good example is an excellent n-type and p-type SWCNTs network film which showed very good PF values, large enough to compete with the best flexible TE materials, respectively 1.5 $mW \cdot m^{-1} \cdot K^{-2}$ and 1.8 $mW \cdot m^{-1} \cdot K^{-2}$, and with a long working lifespan up to three months [83]. In other examples of CNT in organic TE materials, such as the ones referenced above, SWCNTs-polyaniline composite films were developed and reached a PF of 217 $mW \cdot m^{-1} \cdot K^{-2}$, at room temperature,

and showed a good electric generation ability and stability. When assembled in a TE module, it was able to generate 10.4 $mW \cdot m^{-1} \cdot K^{-2}$ of power efficiency, which is superior to most reported results obtained in organic TE modules [84]. CNTs are a good enhancer of TE materials but their usage is still reduced, nevertheless, their potential is worth the research, not just for TE applications but also for many other fields and technologies.

3.4 Superlattices

All the different types of materials mentioned above have different types of advantages, such as improved PF, better performance at room temperature, easy fabrication and low cost, flexibility, etc., thus, sometimes, these benefits come coupled with disadvantages that tend to be the exact opposite of the advantages of other materials, such as low electrical conductivity, toxicity, high cost, difficult production, and many more. Therefore, some approaches, similar in concept to the inorganic-organic composites, try to take advantage of combining materials and uniting their advantages while overlapping their limitations.

One good and common example of these approaches in thin film technology is superlattices. Simply put, a superlattice is a periodic structure of layers of two, or more, thin film materials. They were first discovered by Johansson and Linde in 1925 [85] and, since then, a lot of research around them was done, boosted by the interest in their mechanical properties, which offered more resistant structures and mechanical hardness. But the enhancement of properties wasn't restricted to mechanical properties, quickly, the benefits of superlattices structures in semiconductors structures became apparent. When two different semiconductors with different band gaps are layered successively, it influences the flow of charges and manipulates electrical and thermal properties. This also gave ground to effects such as quantum confinement and quantum wells and dots, which are phenomena that are now useful in modern-day semiconductor structures and technology.

In thermoelectricity exist several common strategies for modulating thin films and their properties, scilicet orientation regulation, magnetic manipulation, strain engineering, formation of two-dimensional (2D) electron gas systems, and superlattices. The latter is relevant for this paper as it utilizes similar systems to be produced and takes advantage of similar properties for the enhancement of raw materials. It's the most advanced and commonly employed of all the strategies referred and it can take advantage of all the material mentioned in this chapter. The most conventional ones are inorganic materials, such as PbTe, Bi_2Te_3, etc.

PbTe-based superlattices are well-researched and common, mostly because this was the first time that the quantum-well effect was verified experimentally, and it increased the ZT [86]. In another study, PbTe/Te superlattices were fabricated and were able to increase the value of ZT at 300 K of bulk PbTe, from 0.37 to 0.52, via scattering mechanisms for the Seebeck coefficient manipulation with the introduction of the Te layers [87]. With the introduction of quantum dots (QD), a further higher ZT of approximately 0.9 was achieved in a PbTe/$PbSe_{0.98}Te_{0.02}$ superlattice [88], but this wouldn't be the final value delivered. Through Bi-doping and Na-doping, the PbTe/PbSeTe quantum dot superlattices (QDSP) showed n-type and p-type conduction behaviour and the n-type QDSP presented an impressive ZT of approximately 1.6 at 300 K and 3 at 550 K, while the p-type superlattice presented an, also remarkable, ZT of 1.1 at 300 K [89]. Despite these impressive results, some data turned out to be unreliable due to inaccurate carrier concentration measurement instead of confinement effect. The re-evaluation of the results showed a 25% and 35% decrease in the mobility of the n-type and p-type PbTe/PbSe nanostructure, respectively. Although this causes a diminish in the PF, the Seebeck coefficient maintained its value for both samples, and the significant decrease of lattice thermal conductivity ensures a higher ZT for these samples when compared to bulk PbTe [90]. Since then, the interest in PbTe-based superlattices decreased significantly, mostly due to the discovery of better solutions.

Bi-Te composites are also a big part of superlattice technology. Intending to develop a good TE generator, a system based in a Bi_2Te_3/Sb_2Te_3 superlattice reached a ZT value of approximately 2.4 along the cross-plane direction at room temperature, through control of the transport of phonons and electrons in the superlattices, which represents a much greater value than the one's found in the bulk material. This ZT value surpasses the value of 1.5 at 300 K of the $Bi_2Te_3/Bi_2Te_{2.83}Se_{0.17}$ superlattice because of the intermixing at the interface, which causes phonon interference to lower, resulting in a higher thermal conductivity [91]. Although a 2.4 ZT value is splendid, it was achieved using metalorganic chemical vapour deposition (MOCVD) which, even though it allows a good and controlled deposition of complex materials such as these, utilizes precursors very hazardous and toxic and it generates exhaust equally toxic, making it a non-ideal deposition method for common applications. In addition, the difficulty of replicating this value with other deposition methods becomes a hindrance because common, safer, and low-cost techniques, such as physical and chemical deposition processes, cannot replicate such values.

Silicon-germanium (SiGe) is an alloy commonly used in modern electronics, such as transistors and solar cells, as a semiconductor material. It is somewhat sustainable and easy to be processed and has been commonly applied in radioisotope TE generators, being mostly used as a TE material for high-temperature applications, typically higher than 1000 K. In its bulk form, it has presented an optimized

value for ZT of 1.3 at about 1173 K, for the n-type [92], while the p-type showed a ZT of 0.95 for the same temperature [93]. Contrarily to others, SiGe-based superlattices have achieved a considerable decrease in thermal conductivity. Whether it was Si/Ge [94], Si/SiGe [95], Ge/SiGe [96] or SiGe/SiGe [97], all superlattices developed with this compound showed lower thermal conductivity than bulk materials, implying great potential in practical applications. In terms of electrical properties, fewer investigations have been performed, mostly due to difficulties in measurement. Even so, the creation of Si/Ge QDSL results in improved mobility, greatly reduced thermal conductivity and increased ZT value by several orders, culminating in a promising TE structure [94]. Similarly, the introduction of doping and nanostructures in the other types of superlattices enhances the TE performance, but the lack of electrical studies and mostly the high-temperature working conditions limit their implementation.

As a representative of antimonide-based superlattices, GaSb/InAs superlattices are widely used as a cooling material in infrared detectors due to their excellent Seebeck coefficient at low temperatures [98]. However, the investigations on the electric properties of these superlattices are scarce and therefore, there are no experimental results of ZT values reported. Nonetheless, this structure shows good thermal performance, hence its common presence in cooling systems, with values of thermal conductivity ranging from 1 $W \cdot m^{-1} \cdot K^{-1}$ to 8 $W \cdot m^{-1} \cdot K^{-1}$ from 13 to 300 K [98]. Even though this represents a good solution, the lack of abundant material and difficulties in deposition limits interest in these superlattices, resulting in insufficient research.

In a nutshell, superlattices go hand in hand with other types of structures in the way they try to take advantage of the material's inert properties to develop an efficient TE structure. Some examples were presented for all ranges of temperatures, antimonides type II superlattices such as GaSb/InAs are suitable for low temperatures, Bi_2Te_3/Sb_2Te_3 superlattice equipment ought to be used at room temperature, PbTe/PbSeTe structures work well in a medium-high temperature environment and Si/Ge superlattices are useful in high-temperature TE devices.

4. Zinc Oxide

Zinc oxide (ZnO) is a well-known inorganic compound quite common in modern electronics, mostly due to its abundance and versatility. It has a direct band gap, and it crystallizes in the hexagonal wurtzite structure, displaying an intrinsic n-type conductivity. Furthermore, added to the possible conductivity characteristics, the optical properties of ZnO make it a viable solution for TCO technology, but its naturally high electrical resistivity is a constraint that is usually countered by doping. Most common dopants are elements from the third group, but controlling the conductivity remains a major issue because even small concentrations of impurities can affect the electrical and optical properties of semiconductors. Nonetheless, due to its unique and fascinating features, ZnO is considered an appropriate substitute for gallium nitride (GaN) in several types of applications, and it has the possibility of targeting others such as TE technology.

4.1 Relevant properties and applications

4.1.1 Crystal structure and lattice parameters

Like some other of the group-II-VI binary compound semiconductors, ZnO crystallizes in a hexagonal wurtzite structure, where each anion is surrounded by four cations at the corners of a tetrahedron, and vice versa. Although at ambient conditions, the thermodynamically stable phase is wurtzite, a cubic zinc-blende ZnO structure can be stabilized by growth on cubic substrates, and a rocksalt structure may be obtained at relatively high pressures. The wurtzite structure's unit cell is characterized by two lattice parameters, *a* and *c*, respecting the c/a = 1.633 ratio. For the ZnO structure at room temperature, experimental measurements were performed, and the lattice constants mostly range from 3.2475 to 3.2501 Å for the *a* parameter and from 5.2042 to 5.2075 Å for the *c* parameter [99]. The c/a ratio varied in a slightly wider range from 1.593 to 1.6035.

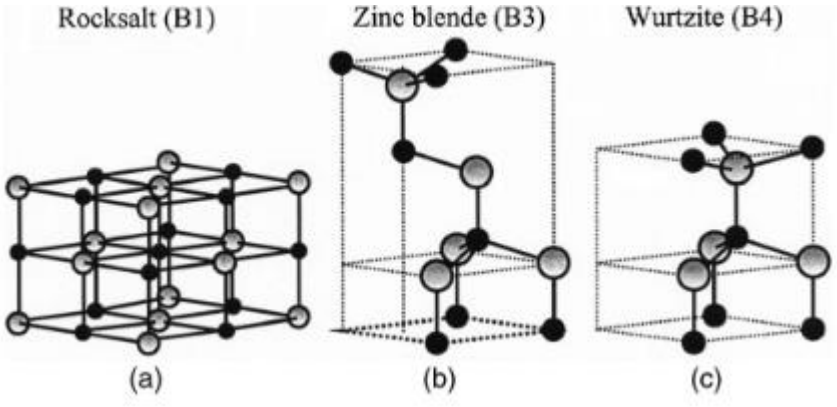

Figure 2: Stick and ball representative of ZnO Crystal structures: (a) cubic rocksalt (B1), (b) zinc blende (B3), and (c) hexagonal wurtzite (B4). The shaded grey and black spheres denote Zn and O atoms, respectively.

4.1.2 Thermal properties

The lattice parameters of semiconductors are temperature dependent and quantified by thermal-expansion coefficients, and they increase with the increase in temperature. Thermal conductivity, which is a kinetic property determined by the contributions from the vibrational, rotational, and electronic degrees of freedom, is an extremely important material property when high-power/high-temperature electronic and optoelectronic devices are considered [99]. Furthermore, it is a crucial characteristic for TE applications, and it can compromise the viability of this material's usage. Heat transport is associated with phonon-phonon scattering, and therefore it is directly affected by defects, such as vacancies or impurities. Here lies a solution to decrease the thermal conductivity by doping if the application requires it. The overall thermal conductivity generally decreases with increasing carrier concentration, because the decrease in the lattice component of the thermal conductivity due to increased phonon scattering from both the impurities and free electrons outweighs the increase in the electronic contribution to the thermal conductivity. Bulk ZnO presents high thermal conductivity and studies found that there's a direct relation to surface roughness, more specifically that higher roughness tends to result in lower thermal conductivity, so different points of the same surface and different surface treatments showed different results for thermal conductivity, with relevant differences [99]. Because the conductivity of ZnO thin films is very sensitive to the exposure of the surface to various gases, there have been instances where this was used to produce cheap sensors, making ZnO suitable for gas sensing technology [100].

Although the high thermal conductivity of ZnO is not advantageous to TE technology, it makes it useful as an additive in specific areas, for example, it is added to rubber for tires to handle the heat generated by the friction of motion, as a high thermal conductivity means high efficiency of heat removal

during operation [101]. But, when it comes to applications in electronics, although it can be useful in heat dissipation, high thermal conductivity can be an obstacle for TE devices.

In any case, a recent study showed that a monolayer of ZnO has a significantly lower thermal conductivity that the bulk form, specifically of 4.5 $W \cdot m^{-1} \cdot K^{-1}$, where the phonon transport is affected by the monolayered structure and causes its decrease [102]. For TE applications, it is still necessary to decrease this value and the main solution tends to be doping, but the choice of dopant must not negatively affect other properties, such as optical and electrical, or the material will not be viable for TCO applications.

4.1.3 Electrical properties

As a direct and large band gap material, ZnO is attracting a lot of attention for a variety of electronic and optoelectronic applications, because the large band gap comes with advantages associated including higher breakdown voltages, the ability to sustain large electric fields, lower noise generation, and high-temperature and high-power operation [99].

Although ZnO shows an intrinsic n-type conductivity, in recent years, it has become a target of interest due to its semiconductor properties as researchers try to control the unintentional n-type conductivity and achieve p-type conductivity [101]. This would mean that ZnO could achieve good values of electrical conductivity and be used in TE applications. But, once again, in its natural form, ZnO does not possess good enough electrical properties to rival other semiconductors. Nonetheless, the doping solution can increase its value and produce a decent material for TE devices.

4.1.4 Optical properties

ZnO shows a direct and wide band gap of 3.44 eV at low temperatures and 3.37 eV at room temperature [103]. This enables applications in optoelectronics in the blue/UV region, including light-emitting diodes, laser diodes and photodetectors [99,101,104]. Furthermore, this allowed for optically pumped lasing to be reported in ZnO, with some examples in thin films and platelets [105,106]. One particularly interesting feature is the high exciton binding energy, which, at 60 meV, should ensure that excitonic emission mechanisms are significant at temperatures well above room temperature. This, in turn, offers the prospect of practical lasers with low thresholds even at high temperatures [105]. Also, ZnO exhibits luminescence in the visible region, more specifically the green band, manifesting peaks at around 500-530 nm, but the cause of this is still a controversial topic. One explanation emerges from oxygen vacancies [99], but other justifications have been considered. Still, this particular

characteristic can be useful, for example, in vacuum fluorescent and field emission displays [101] and, additionally, the luminescence can be tuned to other colour bands by doping [99].

ZnO crystals and, in particular, thin films exhibit second and third-order non-linear optical behaviour, suitable for non-linear optical devices. The linear and non-linear optical properties of ZnO depend on the crystallinity of the samples. ZnO films grown by laser deposition, reactive sputtering and spray pyrolysis show strong second-order non-linear response [101].

Summarizing, ZnO shows great potential and is commonly used in optoelectronic devices due to all kinds of advantages, from luminescence to laser phenomena, and has the added benefit of being able to retain transparency in thin film form, making it a suitable solution for TCO development.

4.1.5 Mechanical properties

The mechanical properties of materials conjugate several concepts, like hardness, stiffness, piezoelectric constants, yield strength, etc. In terms of hardness, ZnO is usually at the centre of the Mohs' scale, with around 5.0 GPa, and it is not the material that stands out the most because of this lack of strength and hardness [99]. Its stiffness accompanies this trend, as it is not a material that has the best stiffness, but it does not show flexibility.

On the other hand, the low symmetry of the wurtzite crystal structure combined with a large electromechanical coupling in ZnO gives rise to strong piezoelectric and pyroelectric properties [101]. There are many examples of piezoelectric ZnO films with uniform thickness and orientation that have been grown in a variety of substrates through different deposition techniques, with sputtering being the most ordinary and efficient one [107–109], but other examples like chemical deposition are also prevalent [110]. The piezoelectric properties of ZnO are used in many types of applications, but generally, they're applied in modern electronics as sensors, transducers and actuators.

4.1.6 Growth and substrates

Due to these characteristics, the growth of ZnO thin films has been extensively studied for many types of devices on various kinds of substrates, such as glass, sapphire, and diamond [99]. It's a very versatile material when it comes to deposition as it is often deposited by several different techniques, namely pulsed laser deposition (PLD) [111], molecular beam epitaxy (MBE) [112,113], atomic layer deposition (ALD) [114], chemical vapour deposition (CVD), sol-gel synthesis [115], spray pyrolysis [116], and physical vapour deposition (sputtering), but earliest reports utilized magnetron sputtering [117,118]

and CVD [119,120]. Throughout the evolution of techniques and studies on ZnO, sputtering remained the most commonly used technique for ZnO thin film growth due to low cost, simplicity, and low operating temperature [99].

4.2 Doping of ZnO

Aiming to fully control and take advantage of ZnO's promising properties, researchers resorted to doping to effectively produce both high-quality n-type and p-type ZnO. Attaining proper doping and enhancing its properties is indispensable for making ZnO a suitable solution in optoelectronic device applications, including TE applications. However, several difficulties in both doping types created different setbacks for this material's implementation.

Usually, n-type doping of ZnO is relatively easy compared to p-type doping, because ZnO is naturally an n-type semiconductor. Group-III elements, like Al and Ga, can act as substitutional elements for Zn and group-VII elements, like chlorine (Cl) and iodine (I), can serve as substitutional elements for oxygen (O) and be used as n-type dopants. Doping with Al, Ga, and In has been attempted and achieved by many groups, resulting in high-quality, highly conductive n-type ZnO films [99] , and these elements have been tested to create materials for TE applications. Al is a cheap, abundant and non-toxic material [121], and aluminium-doped zinc oxide (AZO) has been commonly researched for several practical applications, such as transparent electrodes, where it was crucial in achieving low electrical resistivity and high optical transmittance. Transparent and conductive ZnO:Al thin films were deposited by pulsed direct current (DC) magnetron sputtering and it was shown that a lower argon (Ar) pressure leads to lower film electrical resistivity. Additionally, post-treatment of hydrogen plasma proved to be very efficient in enhancing the electrical properties of these films, achieving an electrical resistivity of 1.2 $\mathrm{m\Omega \cdot cm}$ and a transmittance of approximately 80% in the visible region for a film with 200 nm of thickness. In terms of TE properties, the study also showed a maximum PF of 7.27 $\times 10^{-2}$ $\mathrm{mW \cdot m^{-1} \cdot K^{-2}}$ at 350 K [122]. But the maximum power output of Al-doped ZnO is 2.3 nW, for a temperature gradient of 20 K near room temperature yielding a ZT of above 0.1, which is much higher than other ZT values found before the study, at least for room temperature [123]. A more recent examination showed that nanostructured AZO could reach a ZT value up to 0.44 at 1000 K, making it 50% larger than the non-structured counterpart [124]. Finally, Al-doping even went beyond the hard substrates and thin films were deposited on a flexible substrate, where an n-type AZO and p-type Zn-Sb-based thin film TE generator reached a power of 246.3 μW when the temperature difference is 180 K [125]. As shown by these examples, Al is typically the most versatile and

common choice among group-III elements for n-type doping of ZnO, but Ga and In are decent rivals for the same purpose. Gallium-doped zinc oxide (GZO) films grown by CVD reported resistivities as low as 0.12 mΩ·cm and proved that the increase in doping levels would not affect the film's optical transmittance [126]. More recently, a study produced GZO films which could achieve a PF up to 1.4 $mW \cdot m^{-1} \cdot K^{-2}$ at 850 K, and a TE generator module using GZO was fabricated to attain a maximum power output of 230 nW at ΔT = 138 K [127]. Similarly, in a study of Indium-doped zinc oxide (IZO), an optical transmittance in the order of 80% was obtained for all films fabricated, and the lowest resistivity value was 0.045 Ω·m [128]. Summarizing, n-type doping with third-group elements potentializes ZnO thin films for TE and TCO applications, as the electrical resistivity can be decreased with finetuned doping without compromising the transparency of the film and, in some cases, it can produce a decent ZT value, making it possibly useful for practical applications.

P-type is not as straightforward as n-type doping because it is very difficult to obtain p-type doping in wide band gap semiconductors and these difficulties can arise from numerous causes. Dopants may be compensated by low-energy native defects, or it can be due to low solubility of the dopant in the host material, or even deep impurity levels can also represent a source of the doping problem, causing significant resistance to the formation of shallow acceptor level [99]. Known acceptors in ZnO include group-IA elements such as lithium (Li), Na, and potassium (K), or group-IB elements like Cu, and Ag, and group-V elements such as nitrogen (N), phosphorus (P), and arsenic (As). However, many of these elements form deep acceptors and do not contribute significantly to p-type conduction. Group-V elements have been catalogued as the most promising dopants for p-type ZnO, although theory suggests some difficulty in achieving shallow acceptor levels [129]. With doping with elements from group-I, it is intended to substitute these elements for Zn sites and, when doping with group-V elements, it is expected that they occupy the O sites. However, group-I elements tend to occupy the interstitial sites rather than substitutional sites, in part mitigated by their small atomic radii, and, therefore, act mainly as donors instead [99]. Additionally, some elements from this group, like Na and K, have significantly larger bond lengths than the ideal Zn-O bond length, inducing lattice strain, increasingly forming native defects such as vacancies which compensate the very dopants, making it counterproductive. Similarly, some elements of group-V have the same effect, possessing larger bond lengths. A study on the effect of bismuth (Bi) doping in the structure of ZnO concluded that the large Bi^{3+} ions do not enter the ZnO lattice and are instead likely located in the disordered environment at the ZnO grain boundaries. This conclusion also explained why, in a previous related study, Bi-doping resulted in a decrease of the Seebeck coefficient despite a decrease in electrical resistivity [130], effectively showing that sometimes doping negatively

affects the TE performance of ZnO. Nevertheless, other elements of group-V have been extensively studied because they can achieve p-type doping, by effectively infiltrating the ZnO lattice, namely nitrogen (N). Many studies focused on N-doped ZnO films have successfully achieved p-type doping with high nitrogen concentrations and decent values for hole concentration, mobility and resistivity, through a big variety of deposition methods [131–137]. Some of these corroborated that, Zn-poor samples are generally of p-type because the combination of a high concentration of zinc vacancies plus the insertion of nitrogen and the coexistence of oxide and peroxide groups can lead to the stabilization of positive charge carriers. Furthermore, since the substituting nitrogen is not shallow, the researchers suggest that zinc vacancies play a crucial role in the p-type nature of the material. Additionally, undesired forms of nitrogen will critically reduce the efficiency of nitrogen doping and compensate for the acceptors, so the compensation must be greatly suppressed for high-quality p-type conduction to be achieved [138]. Consequently, some groups transferred their efforts from thin films to nanostructures, producing several structures such as nanoparticles and nanowires, and the results show that these structures can accommodate for an easier-to-achieve p-type conduction in ZnO doping. However, the relatively high resistivity and low hole mobility have not been substantially improved [138]. Even though N has been one of the most popular materials for p-type doping of ZnO, it has not shown promising results for the development of a good TCO for TE applications. Other group-V elements have been studied, and a promising, yet also commonly researched element with good potential is Antimony (Sb).

4.2.1 Antimony-doped Zinc Oxide

Antimony-doped zinc oxide (SZO) is a possibly good solution for achieving p-type conduction in ZnO thin films. Contrarily other counterparts, like Bi, when Sb is used in ZnO doping, it can infiltrate the lattice structure, although, due to the large radius of its ions, unlike N-doping, it tends to occupy de Zn sites [138]. Either way, Sb has been used to achieve p-type conductivity and to produce transparent and conducting films with decent TE properties.

Table 1 resumes most of the recent studies performed on SZO regarding electrical conductivity and TE properties. It is proven that Sb allows for achieving p-type conductivity, both in thin film technology and nanostructuring, with decent electrical properties, namely mobility, carrier concentration and resistivity. Nevertheless, the lack of study of the TE and optical properties of SZO becomes apparent and its possible use for TCO technology remains vaguely unanswered, as only recent studies focused on the Seebeck coefficient and PF and didn't obtain the most promising results. The focus of this paper is to fill

that vacant space in research and perform a full analysis of the optical, electrical and TE properties of SZO.

Table 1: Resume of the recent studies performed on SZO and their respective properties.

Methods	**Transmittance** ($\%\ \boldsymbol{in\ Vis}$)	**Mobility** ($\boldsymbol{cm^2/V\cdot s}$)	**Resistivity** ($\Omega\cdot\boldsymbol{cm}$)	**Seebeck Coefficient** ($\mu\boldsymbol{V/K}$)	**Power Factor** ($\mu\boldsymbol{W/m\cdot K^2}$)	**Carrier Concentration** ($\boldsymbol{cm^{-3}}$)	**Conductivity**	**Sample type**	**Year**	**REF**
Electron-Cyclotron-Resonance MBE	-	20.0	0.2	-	-	1.7×10^{18}	p-type	film	2005	[139]
PLD	-	1.23	3	-	-	2.3×10^{18}	p-type	film	2007	[140]
RF Magnetron Sputtering	-	20.0×10^{-3}	0.042	-	-	7×10^{21}	p-type	film	2010	[141]
Spray Pyrolysis	75	54.05	0.185	-	-	6.25×10^{17}	p-type	film	2015	[142]
Oxidative Evaporation	-	2.944	0.05	-	46.79	2.25×10^{20}	p-type	film	2018	[143]
Sol-gel and hydrothermal methods	-	1922×10^{4}	2.07×10^{-3}	-	-	0.16×10^{19}	p-type	nano structure	2019	[144]
DC Magnetron Sputtering	82	-	-	~-160	406	-	n-type	film	2022	[145]
Magnetron Sputtering	-	-	>100	56	0.2	~1025	n-type and p-type	film	2023	[146]

5. EXPERIMENTAL DETAILS

5.1 Film production

Undoped ZnO and SZO thin films were prepared by a custom-made magnetron sputtering system conceived at the Centre of Physics of the University of Minho (see Figure A.1 for the setup's schematic). A confocal geometry was associated with two circular magnetrons, each with a diameter of 10 cm. One was a target of ZnO with 99.99% purity fabricated by FHR Anlagenbau GmbH (Germany), and the other was an Sb target also with 99.99% purity fabricated by Photon Export. A series of depositions were executed but, before each one, the chamber was evacuated with a primary rotary pump and a turbo molecular pump to achieve a base pressure of around 10^{-4} Pa. The films were deposited on 76 x 26 x 1 mm^3 glass substrates from Normax Lda (Portugal) and four 10 x 10 x 0.5 mm^3 Si substrates, cut from P/B doped Si-wafer <100>, from Siegert Wafers GmbH (Germany), following the schematic in Figure A.2. Before assembling the substrates inside the chamber, they were cleaned with isopropyl alcohol (2-propanol) and acetone in an ultrasonic bath, both for 15 min, removing contaminants on the surface of the substrates that may arise during storage and handling, in order maximize the adhesion at the film/substrate interface. The substrate holders were mounted onto a support controlled by a motor that operated in continuous rotation during deposition to ensure uniformity. The distance between the targets and the substrate was kept at 8 cm and the substrate holder was heated before and during depositions. Research grade Ar with 99.999% purity was used as a working gas to enable plasma formation. Ahead of every deposition, a 3 min of ion etching at 500 V was performed in an Ar atmosphere at a pressure of 1.6 Pa. This process was used to remove oxides and impurities that possibly accumulated and were retained on the surface of the substrates, which could create atomic defects in the substrate, enabling better nucleation of the film during deposition.

The series of depositions started with a dummy deposition of 2 hours for target cleaning (burn) of the ZnO target, which was new. This was followed by a control deposition where the Sb target had no current and was covered with an Al sheet to prevent unwanted interactions with the plasma. Then a series of depositions, of 35 minutes each, were performed where the current applied in the Sb target was gradually increased with steps of 2 mA, starting from 0 mA in the first deposition, 1 mA for the second

and ending with 21 mA. This was the only parameter that suffered variations, as all others were kept the same between depositions, intending to effectively study how it would change doping levels and how that change would affect the thin film properties. Already tested deposition parameters used in other studies in the same setup were followed. Target current density, bias voltage, voltage applied in the ZnO target and Ar flow were fixed at 10 mA·cm^2, - 60 V, 400 V and 40 sccm, respectively, maintaining a working pressure between 18 and 21 mPa. Optically transparent and conducting films were effectively fabricated, and their properties were accordingly studied.

5.2 Characterization methods

Throughout this work, several characterization processes were utilized to properly measure the morphological, electrical, thermal and optical properties of the films. This sub-chapter resumes the techniques and devices used for the testing.

5.2.1 Electrical properties

An in-depth study of the electrical properties of the ZnO:Sb thin films was carried out based on the Hall effect. This effect was first discovered by Edwin Hall in 1879 [147], and it is the development of a transverse electric field in a solid material when it carries an electric current and is placed in a magnetic field that is perpendicular to the current [148]. This electric field is the product of the force that the magnetic field exerts on the moving positive or negative particles that constitute the electric current, which causes a displacement of the moving electric charges, resulting in the accumulation of charge on one side, leaving the other oppositely charged, creating a difference in potential designated the Hall voltage (V_H). With this, it's possible to calculate several electrical properties of interest for this paper, such as carrier concentration (n), conjugating the applied magnetic field (B), the film thickness (t) and the injected current (I), as shown in equation 4.

$$n = \frac{|B| \cdot I}{e \cdot |V_H| \cdot t} \tag{4}$$

Furthermore, it is then possible to calculate the mobility (μ) using equation 5.

$$\mu = \frac{1}{e \cdot \rho \cdot n} \tag{5}$$

Utilizing an Ecopia AMP55T HMS-5000 Hall effect measuring system, with a DC four-point probe apparatus in the Van der Pauw configuration, values for the electrical properties were measured for each

sample of the thin film. These measurements were conducted under atmospheric pressure at room temperature, with an applied magnetic field of approximately 0.560 T. Ten measurements were performed for each Si sample of deposition and an average was computed for each of the significant properties referred above, in an attempt to obtain a more accurate result.

Figure 3: Ecopia AMP55T HMS-5000 Hall effect measuring system for electrical measurements.

5.2.2 Optical properties

Values for optical transmittance and reflectance were acquired through measurements in a Shimadzu UV-2501PC UV-Vis spectrophotometer. The glass samples were analysed in the 300 to 900 nm wavelength range and the average for each quantity was estimated between 400 and 700 nm for posterior calculations and analysis. For the transmittance, primarily a baseline was established using two samples of glass without any film deposited on them. Then one of them was replaced with each sample that needed to be measured while the other served as a reference. As for the reflectance, a baseline was defined using two mirrors and, similarly to the transmittance, one of the mirrors was kept as a reference throughout the measurements while the other was substituted by the samples with the thin film. Finally, with the transmittance spectra and a custom-made software called *Dcalc*, the thickness and optical properties of each sample were calculated. The software utilizes interference patterns to determine the refractive index of the film and, consequently, its thickness and follows the Swanepoel method to determine the optical properties, namely absorption index and band gap [149].

Figure 4: Shimadzu UV-2501PC UV-Vis spectrophotometer for transmittance and reflectance measurements in the Vis/UV range.

5.2.3 Film morphology and composition

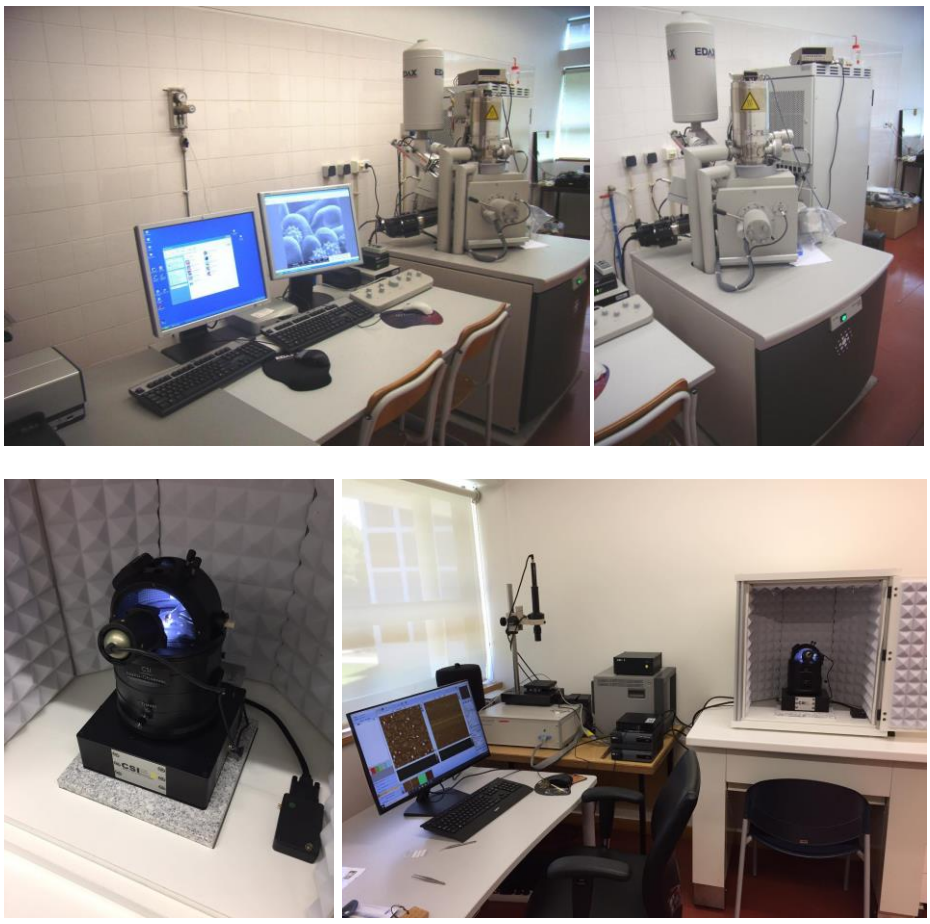

Figure 5: FEI NOVA NanoSEM 200 for SEM analysis, EDAX- Pegasus X4M for EDX analysis (top) and Nano-Observer Atomic Force Microscope for AFM analysis (bottom) [151].

A study on the morphology and cross-section of the thin films was performed with scanning electron microscopy (SEM), performed with an FEI NOVA NanoSEM 200. To perform cross-section imaging, the samples were cut with a diamond tip and fixated in the sample table with double-sided carbon tape.

Atomic force microscopy (AFM) was also used to study the surface properties of the film, namely roughness, on a Nano-Observer Atomic Force Microscope. Several measures of specific samples were taken and, for each sample, two different measurements in two different zones of the film, typically one near the centre and one near the edge were determined. A mean of both values was performed afterwards for a more accurate evaluation.

The surface chemistry of the produced ZnO:Sb films was studied with an XPS spectrometer (Kratos Axis-Supra instrument, at 3Bs Group, University of Minho) equipped with a monochromatic Al-Kα X-ray radiation source (1486.6 eV) operated at an X-ray power of 225 W. The photoelectron spectra were collected at the take-off angle of 90° with the sample surface by means of a hemispherical electron energy analyser operated in the constant analyser energy lens mode (CAE). The pass energy of 160 eV and 40 eV was used for the survey and high-resolution spectra, respectively. The binding energy was referenced by setting the binding energy of the C1s hydrocarbon peak (the most intensive component of the C1s spectrum) at 284.8 eV. An electron flood gun was used to compensate for surface charging effects. Furthermore, to improve the composition study, energy-dispersive X-ray spectroscopy (EDX) was performed in an EDAX- Pegasus X4M.

5.2.4 Structural properties

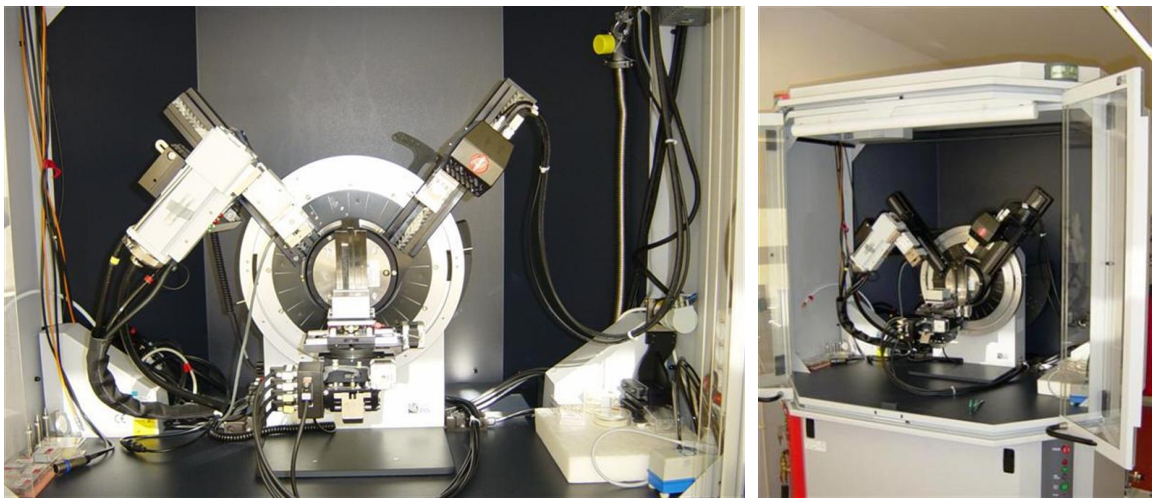

Figure 6: Bruker AXS D8 Discover diffractometer for XRD analysis [151].

X-ray diffraction (XRD) analyses were performed to study the crystallographic structure of the thin films using a Bruker AXS D8 Discover diffractometer operated in $\theta - 2\theta$ geometry with CuKα radiation. XRD patterns were obtained with a step size of 0.02 and an integration time of 1.5 s. Afterwards, with the help of the software *Fityk*, the XRD diffraction patterns were analysed.

5.2.5 Seebeck coefficient

The Seebeck coefficient is one of the most important properties of this project. Its evaluation was made using custom-made equipment that consisted of three main parts: the chamber, the pump and a custom-made controlling software and hardware system. The pump ensured a low vacuum of approximately 1 Pa inside the chamber upon analysing. Inside the chamber were placed the holding system and the temperature control setup. Two Peltier devices (Quick-Ohm Kupper & Co. GmbH) operate as heater and cooler for the edges of the sample, applying their effect in a 25 x 75 mm^2 area. These devices ensure the difference in temperature necessary for calculating the Seebeck coefficient, and the potential difference is measured using a 2-probe contact geometry, proven to be efficient even with high temperatures [150].

For each sample, the thermal gradients applied on the film deposited on the glass varied between 35 and 60 °C, with a step of 5 °C, resulting in six measures for increasing ΔT. For each measurement, 10 minutes for stabilization were given to obtain a good and coherent value. These values are controlled and registered by the third part of the system, the hardware and software, where a custom-made interface is responsible for controlling the applied temperature in each Peltier device, controlling its evolution along the analysis and registering each respective potential difference. After the experiment, and with all the values registered, the obtained ΔV values were plotted as a function of ΔT and linearly fitted to determine the slope, and subsequently the Seebeck Coefficient, similar to other applications of this same system [59].

6. Results and Discussion

In total, 13 samples were deposited for this study. The first one, an undoped ZnO thin film (ZnOX) served as a control sample, as it was deposited with the Sb target covered so it would not affect the normal deposition of ZnO. Then, the rest of the samples were deposited with normal conditions and an increasing current was applied to the Sb target. This allowed studying the effect that the deposition parameters, namely the current applied, have on the Sb integration. Furthermore, it allowed examining the influence of Sb doping in the structural, optical and electrical properties of the ZnO thin films. Additionally, the comparison between the first film and the one where no current was applied in the Sb target allowed verifying if the presence of the Sb target affects the deposition and film parameters, even with no current applied to its target.

Table 2: Produced samples and their deposition process parameters.

Sample	**Sb Target Current (mA)**	**Initial Conditions**		**During Deposition**	
		Temperature (°C)	Pressure (mPa)	Temperature (°C)	Pressure (Pa)
ZnOX	0	49	0.32	78.5	0.19
ZnO:Sb00	0	70	0.12	89.5	0.20
ZnO:Sb01	1	50	0.05	73.5	0.20
ZnO:Sb03	3	51	0.08	75.0	0.20
ZnO:Sb05	5	48	0.09	75.5	0.20
ZnO:Sb07	7	50	0.07	75.0	0.22
ZnO:Sb09	9	51	0.08	72.0	0.20
ZnO:Sb11	11	54	0.09	59.0	0.21
ZnO:Sb13	13	54	0.12	69.0	0.21
ZnO:Sb15	15	53	0.09	65.5	0.21
ZnO:Sb17	17	48	0.10	73.0	0.22
ZnO:Sb19	19	52	0.12	72.5	0.20
ZnO:Sb21	21	47	0.11	71.0	0.19

*Constant parameters in all depositions: Bias voltage (-60 V), Current applied to the ZnO Target (400 mA), Ar Flow (40 sccm).

For sake of simplicity, the title of each film corresponds to the current applied in the Sb target during deposition (Zno:SbXX = the film deposited with XX current applied in the target, in mA). Table 2 summarizes the depositions that were made for a quick consultation of the deposition parameters.

6.1 Compositional and structural analysis

Starting with the SEM analysis, a couple of samples, namely the control sample ZnOX and the doped samples ZnO:Sb00, ZnO:Sb01, ZnO:Sb11, and ZnO:Sb21, were chosen to be tested as they represent the control, start, middle and end of the sample sequence, to verify the evolution of the sample properties through increasingly higher doping parameters, because it was not possible to analyse all the samples. As result, several pictures of the cross-section and surface of each sample were taken (see Figure B.1). With the data, an average thickness was measured and calculated for each film. For the rest of the samples, an estimation was calculated with a logarithmic regression, which was the one that adjusted better to the obtained results, and the plots are represented in Figure 7. Even though this estimation is not perfect, it shows a steady increase in thickness as the doping level increases, which is expected.

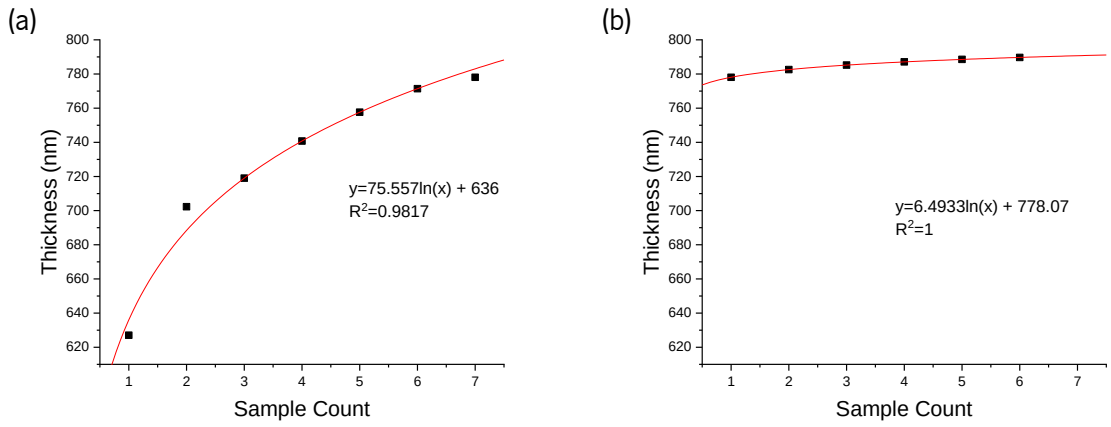

Figure 7: Logarithmic regression for the (a) Zno:Sb01 to Zno:Sb11 and (b) Zno:Sb11 to Zno:Sb21.

Afterwards, with the transmittance spectra, the thickness of each film was calculated with the software *Dcalc*. The results showed an increase for each sample when compared with the SEM cross-section measurements and calculations. Nevertheless, that difference never reached 100 nm and only 5 samples had a difference larger than 50 nm. Most of the results matched the SEM measurements with just a small difference. This corroborated the results from the SEM analysis and calculations as the largest differences can be attributed to calculation errors in the software or imperfections of the film due to imperfect deposition that affected the transmittance and its spectrum, but the most probable one would

be behind the *Dcalc* calculations as it performs several approximations when estimating refractive index, etc. Table 3 resumes the results.

Furthermore, still with the *Dcalc* software, the Tauc plot of each sample was printed, and the energy band gap was calculated (see Figure B.2). The energy band gap averaged at around 3.25 eV, which is lower than the 3.37 eV of ZnO, at room temperature, even than just slightly, showing the effect of the Sb doping in the films.

Table 3: Thin film thickness by sample from SEM measurements and calculations, and from *Dcalc* calculations alongside the respective difference between the results. The energy band gap of each film obtain in the *Dcalc* software is also tabled.

Sample	**Thickness (nm)**			**Energy band gap (eV)**
	SEM analysis	*Dcalc* calculations	Difference	
ZnOX	578.47	597	18.53	3.26
ZnO:Sb00	627.03	707	79.97	3.26
ZnO:Sb01	702.30	710	7.70	3.25
ZnO:Sb03	719.01	794	74.99	3.25
ZnO:Sb05	740.74	799	58.26	3.25
ZnO:Sb07	757.60	790	32.40	3.24
ZnO:Sb09	771.38	794	22.62	3.26
ZnO:Sb11	778.07	787	8.93	3.25
ZnO:Sb13	782.57	802	19.43	3.25
ZnO:Sb15	785.20	826	40.80	3.24
ZnO:Sb17	787.07	814	26.93	3.25
ZnO:Sb19	788.52	790	1.48	3.25
ZnO:Sb21	789.70	818	28.30	3.24

The same samples selected for the SEM analysis were chosen for the EDX analysis. It was expected to see an increase in the at.% of Sb with the increase in the current applied to the target, meaning that the doping level is higher, but as it is possible to see in Table 4, that does not verify. The at.% of Sb showed very low results and they stayed essentially the same or even decreased when compared with the sample with 0 mA of current applied. This must be related to the fact the limit of solubility of Sb in the wurtzite structure is around ≈0.5 at.%, and further increase in the Sb target current density does not overcome this threshold. The absence of Sb in the control sample verifies that covering the target

prevented impurities, but the ZnO:Sb00 sample shows the presence of Sb, which means that, even with no current applied to the target, its presence still affected the deposition. Nevertheless, even though the at.% is low, it is still relevant and it shows the presence of Sb in the ZnO cell.

Table 4: Zn, O and Sb content in at.% for the samples submitted to EDX analysis.

Sample	Zn (at.%)	O (at.%)	Sb (at.%)
ZnOX	57.06	42.94	-
ZnO:Sb00	57.27	42.26	0.47
ZnO:Sb01	57.42	42.07	0.51
ZnO:Sb11	57.50	42.38	0.12
ZnO:Sb21	57.37	42.29	0.34

Table 5 presents the experimental results of the XPS analysis, more specifically the fitted spectra for the Zn 2p (doublet), O 1s (singlet) and Sb 3d (doublet) core line levels for an undoped sample (ZnOX) and a ZnO:Sb sample (ZnO:Sb21). The composition is approximately stoichiometric for the undoped sample, with a slight deficiency in Zn (48.7 at.%). It should be noted that XPS is only sensible to the topmost atomic layers (≈7 nm below the surface), hence, this slight zinc deficiency may be attributed to some evaporation of this material, which competes with sputtering due to its low melting temperature. For the case of the Sb-doped sample, the sub-stoichiometry is reversed, being the film deficient in oxygen (48.8 at.%) due to the promotion of oxygen vacancies upon Sb doping (1.0 at.%) in the wurtzite structure. The latter value of Sb doping is larger than that was measured by EDX (0.34, in Table 4), since EDX averages the film bulk, while XPS only the topmost atomic layers, hence the registered increase in Sb at the surface, possibly by diffusion processes. From Figure 8 (a) and Figure 9 (a) it can be seen that the shape and position of the $Zn2p_{3/2}$ peak (1021.3 eV) is practically unaltered with doping, being the doublet separation the same (ΔE=23.1 eV), and the peaks full width at half maximum (FWHM, β) are within 1.5 – 1.7 eV. However, for the O1 core line the impact of Sb-doping is readily viewed (Figure 8 (b) and Figure 9 (b)). Since the O 1s core line overlaps with the $Sb3d_{5/2}$ main doublet peak, the fitting of these two core lines presents a challenge. The strategy that was used was to first fit the Sb3d doublet (Figure 9 (c)) and from the position of the lower intensity doublet peak ($Sb3d_{3/2}$), the relative areas between the $3d_{5/2}$:$3d_{3/2}$ (3:2) doublet peaks, the determined spin-orbit splitting (9.6 eV) of these peaks, using the position of $3d_{5/2}$ (530.2 eV) and its FWHM (1.2 eV), it was then possible to fit the O 1s core line (Figure 9 (b)) by forcing the insertion of the $3d_{5/2}$ in its envelope structure (component CSb in Table 5 and Figure 9 (c)). For both

samples, the O 1s core line was fitted with two contributions as follows. For the lower binding energy (529.9 – 530.0 eV) component C1 is ascribed to Zn-O bonds and Sb-O bonds (doped sample), and its position only varies marginally (0.1 eV), with unaltered FWHM. Whereas component C2 (531.6 – 532.0 eV) is attributed to adsorbed oxygen and OH groups, mostly from surface contamination, and C2 was not taken into account to determine film composition. The area of C1 is slightly larger (66%) for the undoped sample, in comparison to the Sb-doped sample (63%).

Table 5: Composition and core line binding energy positions derived from the XPS fits to the ZnO:Sb films data. ΔE is the spin-orbit separation of the Zn 2p and Sb 3d doublets. β is the FWHM of the fitted peaks. A relative area percentage (%) is given for the two O 1s contributions (C1 and C2) with respective FWHM (β1 and β2). CSb in the O1s spectra is attributed to the Sb $3d_{5/2}$ (530.2 eV) doublet peak.

			Zn 2p	**O 1s**	**Sb 3d**
Sample	**Composition (at.%)**		Position / ΔE / (β) (eV)	C1 (β_1) % CSb (β) % C2 (β_2) % (eV)	Position / ΔE / (β) (eV)
ZnOX	Zn	49.7	1021.3 23.1 (1.7)	529.9 (1.1) 66%	-
	O	50.3		-	
	Sb	-		531.6 (1.7) 34%	
ZnO:Sb21	Zn	50.2	1021.3 23.1 (1.5)	530.0 (1.1) 63%	530.2 9.6 (1.2)
	O	48.8		530.2 (1.2) 13%	
	Sb	1.0		532.0 (1.5) 24%	

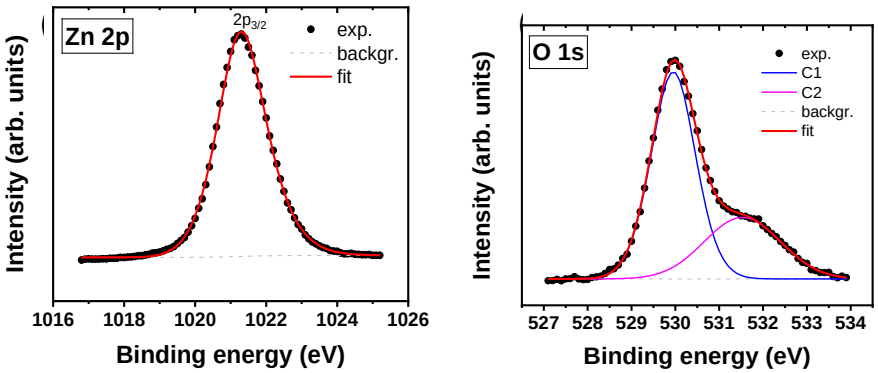

Figure 8: Zn 2p and O1s XPS core lines and respective fits for the undoped ZnO film (ZnOX).

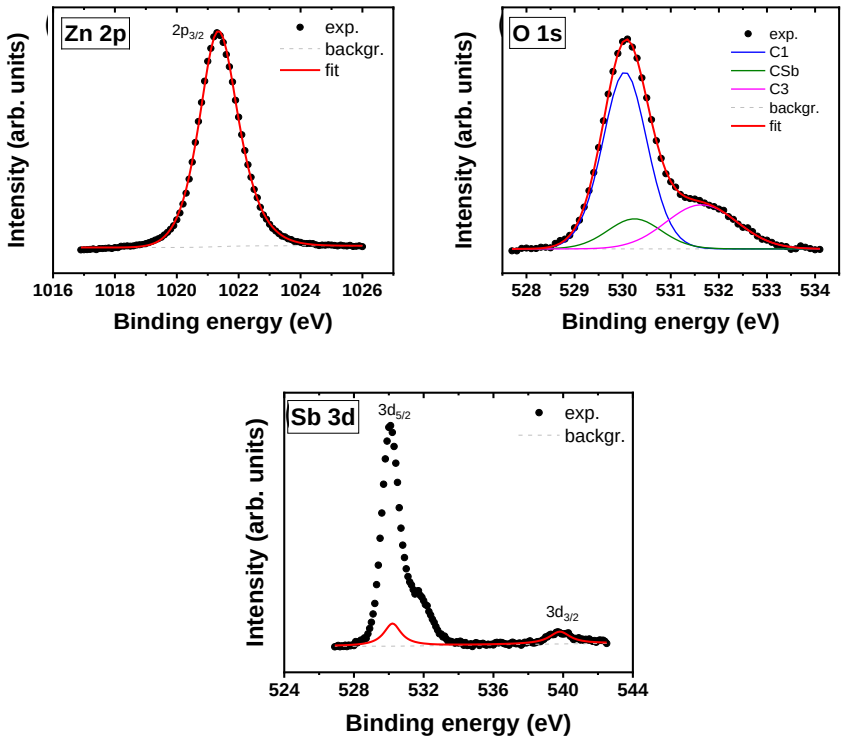

Figure 9: Zn 2p, O1s and Sb 3d XPS core lines and respective fits for the Sb-doped ZnO film (ZnO:Sb21).

As for XRD, because, once again, it was not possible to study all the samples; the ZnOX, ZnO:Sb01, ZnO:Sb03, ZnO:Sb07, ZnO:Sb13 and ZnO:Sb21 thin films were chosen for the study.

Figure 10 shows the XRD patterns of these films, for $25° < 2\theta < 65°$, with an incident angle of 1.5° (glancing angle diffraction). The registered diffraction peaks were assigned to a ZnO phase with hexagonal wurtzite crystal structure, P63mc, and the highest intensity peak, referent to the (002) atomic plane, places itself at around 34.5°, which corroborates with the information from the crystallographic card 1011258 from the ICSD database, which served as a study reference. Furthermore, a small peak

at around 36° appears for the films with theoretical Sb content (see Figure B.3). According to the crystallographic card 1007077, referent to an Fd-3m space group, ZnO:Sb presents a peak around 34.6° for the (311) atomic plane and another peak at around 36.1° for the (222) atomic plane. The appearance of a peak at around 36° for the Sb-doped, and the increase in its intensity the samples deposited with higher current applied to the target, corroborates the increasing doping level as ZnO:Sb becomes more present. Added to the doping confirmation, from Figure 10, the highest (002) peak intensity is associated with the sample deposited with the highest current density; so, the higher presence of Sb improves crystallinity. This is also shown in the SEM images (see Figure B.1), where more highly doped samples also showed better crystallinity. Although these differences are visible, they are not obvious and that is to be expected because, even though there was Sb-doping, the Sb at.% is low.

The results presented in Table 6 show the lattice parameters (*a*, *c*), grain size (g) and full width at half maximum (FWHM), from the XRD analysis and *Fityk* adjustments. The lattice parameters are slightly but not significantly higher than the reference's parameters of 3.22 Å and 5.2 Å for *a* and *c*, respectively, which shows that there's no relevant lattice strain. But, between the control sample (21 nm) and the doped samples (≈25 nm), there's a small difference in grain size and FWHM, where the grains of the doped samples are slightly larger. This fits well with the previous results, as it also shows the effect and presence of Sb. Even more, the uniformity in grain size of all doped samples agrees with the stability of Sb content measured in the XRD analysis.

Table 6: Lattice parameters (*a*, *c*), crystallite grain size (g) and FWHM of the (002) plane peak obtained with XRD analysis and calculated with the *Fityk* software. Additionally, mean roughness (Ra) and quadratic roughness (Rq) are also tabled.

Sample	***a*** **(Å)**	***c*** **(Å)**	**g (nm)**	**FWHM (002) (rad)**	**Ra (nm)**	**Rq (nm)**
ZnOX	3.27	5.25	21	0.0068	4.97	6.35
ZnO:Sb01	3.28	5.25	25	0.0058	4.82	6.35
ZnO:Sb03	3.28	5.24	25	0.0058	9.52	11.84
ZnO:Sb07	3.29	5.24	26	0.0057	5.23	6.59
ZnO:Sb13	3.27	5.24	25	0.0058	8.93	11.21
ZnO:Sb21	3.29	5.24	24	0.0060	9.84	12.10

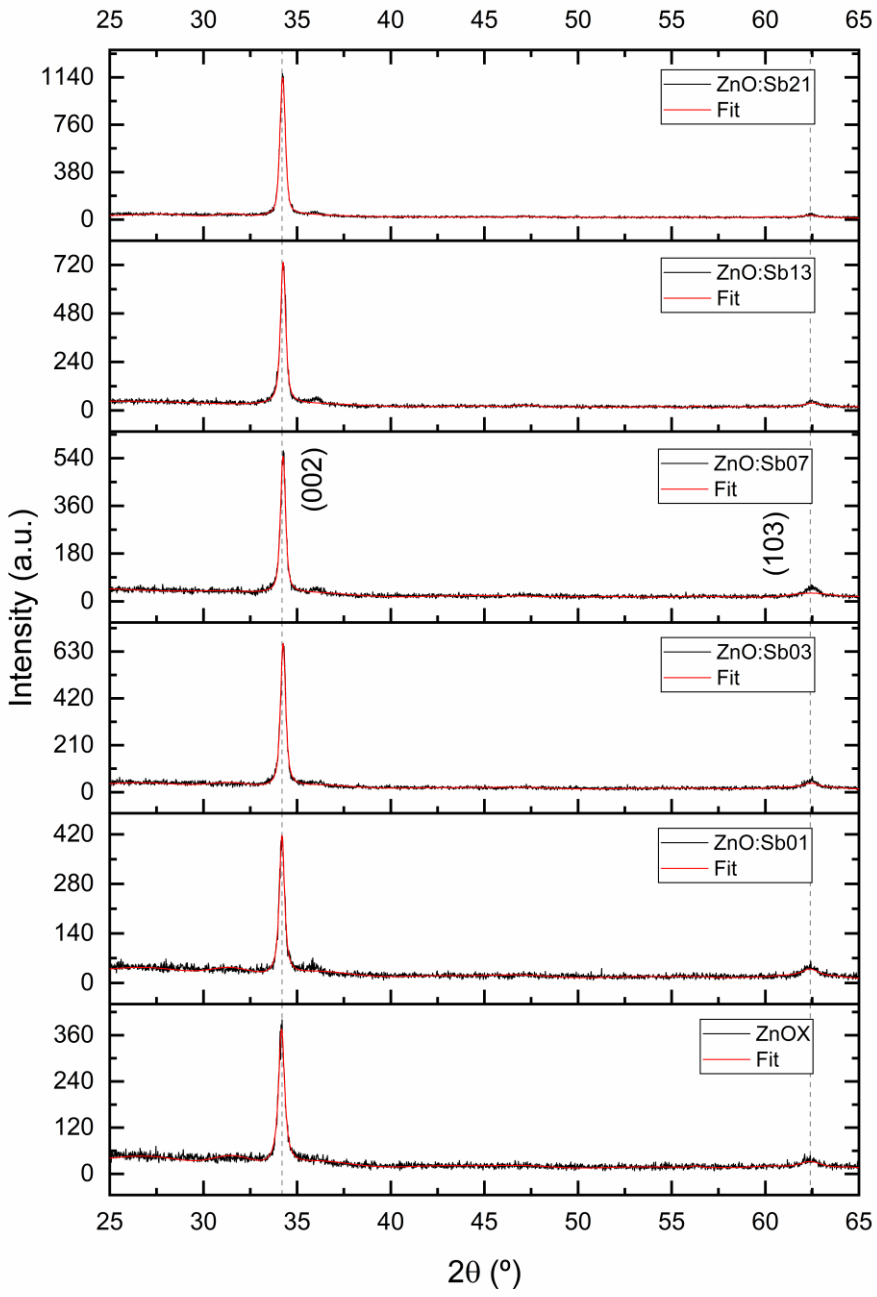

Figure 10: XRD patterns for ZnOX, ZnO:Sb01, ZnO:Sb03, ZnO:Sb07, ZnO:Sb13 and ZnO:Sb21 thin films.

To more accurately analyse the influence of Sb-doping in these properties, the graphs for lattice parameters, grain size and FWHM, as function of Sb at.% were plotted in Figure 11. With these graphs, the data from the samples studied in the EDX analysis was crossed with the data from the XRD analysis, and it was concluded that, for the lattice parameters, there's no significant change and no correlation can be stated, but, for the grain size, there's a tendency for higher Sb content to result in larger particles.

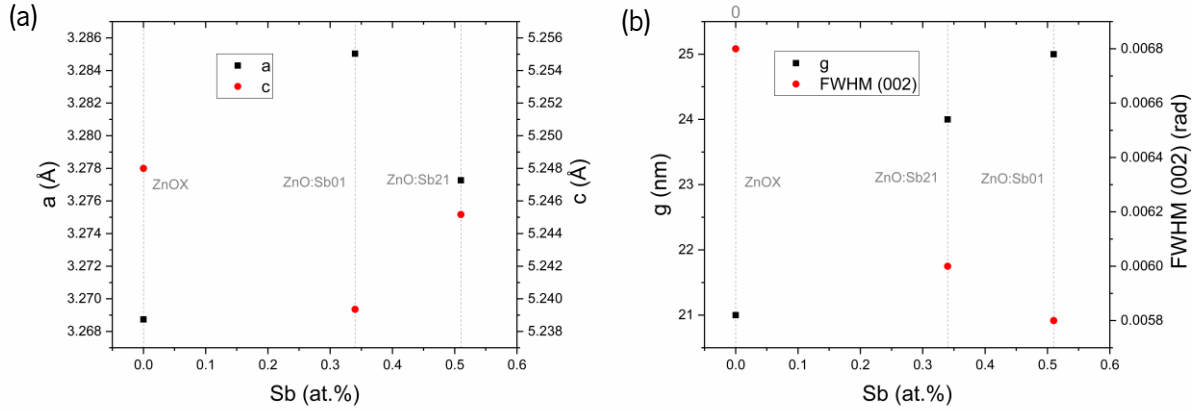

Figure 11: Plots for (a) lattice parameters as function of the Sb content and (b) grain size and FWHM (002) also as function of the Sb content.

Finally, a surface study of the samples was conducted with AFM in a resonance mode of 54 kHz. The respective results are in Table 6 and show the average roughness (Ra) and the quadratic roughness (Rq) of each studied sample, and, because for each film, at least, two measurements were performed, these values are averages. Both roughness values are slightly larger for Sb-doped films (≈9.43 nm and ≈11.72 nm for Ra and Rq, respectively) when compared with the undoped samples (≈4.90 nm and 6.35 nm for Ra and Rq, respectively), except for the ZnO:Sb07 sample which presented only a slight increase (5.23 nm and 6.59 nm for Ra and Rq, respectively), which is visible in the AFM images (see Figure B.4). Its plausible to conclude that Sb increases the roughness of the film, and that there was an error in the ZnO:Sb07 sample making it unviable for this specific analysis. But, looking at Figure 12 (b), this relation stops making sense, as a larger Sb content does not result in a higher roughness value. Nevertheless, higher roughness tends to mean a lower thermal conductivity, so it's expected that the doped films have better TE characteristics, even though this can't be verified due to the lack of study of thermal properties.

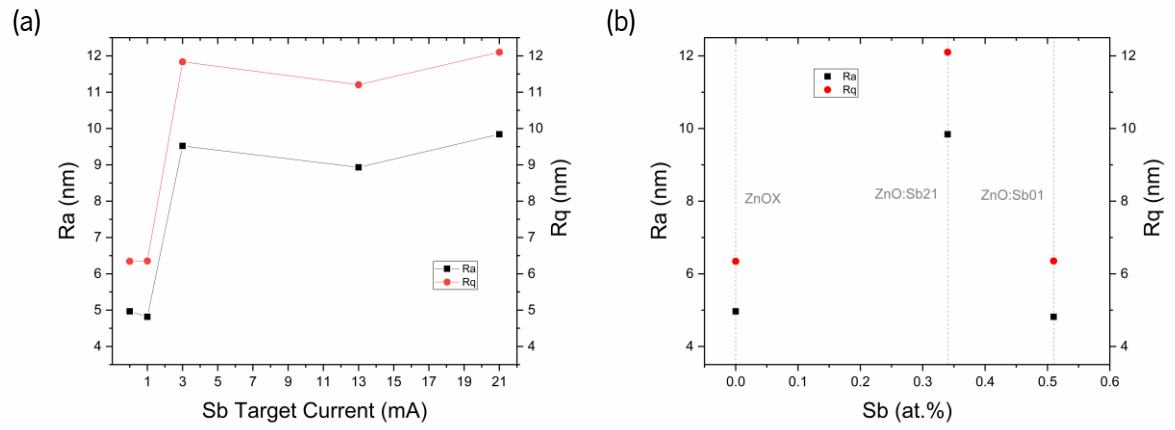

Figure 12: Plot of average (Ra) and quadratic roughness (Rq) as function of (a) the target current applied at the Sb target during deposition and (b) Sb content.

6.2 Electrical properties

With the Hall measurements, electrical resistivity, carrier concentration and carrier mobility were determined, and then tabled and plotted in Table 7 and Figure 13. In the previous analysis, it was observed and verified that there was doping in the samples where the Sb target was subjected to a current density. The resistivity levels of each sample show a similar conclusion. Furthermore, the presence of Sb generates a big decrease in the resistivity, which would imply that higher doping level results in also higher resistivity. The lowest value for resistivity, 0.08 Ω·cm, corresponds to sample ZnO:Sb03, which also showed an increased absolute value of 23.10×10^{18} cm^{-3} for carrier concentration and lower value for mobility of 1.41 $cm^{2}\cdot V^{-1}\cdot s^{-1}$, properties that are all connected. For carrier mobility, doping showed to cause a slight reduction in its value while the opposite happened for carrier concentration. More specifically, the carrier mobility of the undoped samples ZnOX and ZnO:Sb00 was 2.57 and 3.46 $cm^{2}\cdot V^{-1}\cdot s^{-1}$, respectively, but the doped samples showed lower values around approximately 1.50 $cm^{2}\cdot V^{-1}\cdot s^{-1}$, with the lowest value of 0.83 $cm^{2}\cdot V^{-1}\cdot s^{-1}$ corresponding to sample ZnO:Sb13. As for carrier concentration, the absolute base values of the undoped samples of 4.48 and 2.94 $\times10^{18}$ cm^{-3}, for the ZnOX and ZnO:Sb13 samples respectively, had a significant increase with doping, reaching the highest absolute value of 104.08 $\times10^{18}$ cm^{-3}, once again, corresponding to the sample ZnO:Sb13. This samples exhibits the normal correlation between these two quantities, as the increase in carrier concentration comes associated with a decrease in mobility. Furthermore, this sample also shows a reduced electrical resistivity of 0.18 Ω·cm and, although this does not represent the lowest value, it is more than likely linked to these other electrical properties. Finally, the negative nature of the carrier concentration shows that the films have n-type conductivity, preserving this inherent characteristic of the ZnO.

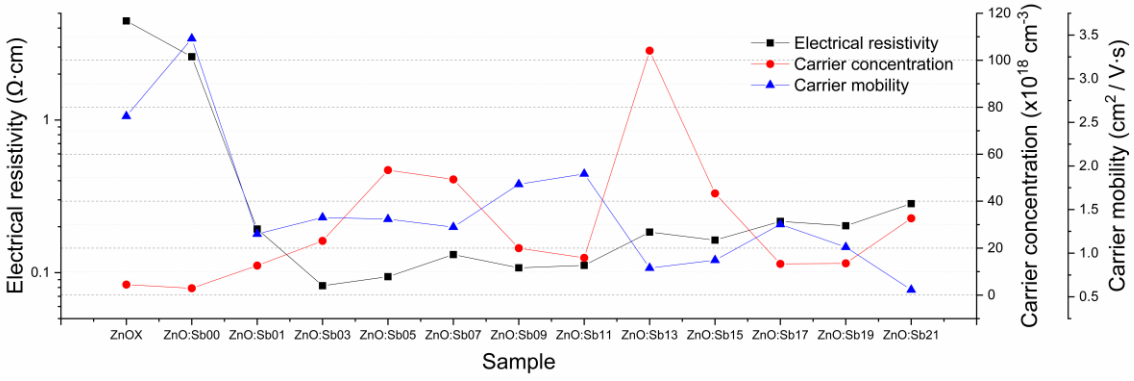

Figure 13: Electrical resistivity and carrier concentration and mobility as function of the sample.

Table 7: Electrical properties of each sample, namely resistivity, conductivity, carrier concentration and mobility.

Sample	Electrical Resistivity $(\Omega \cdot cm)$	Carrier Concentration $(\times 10^{18} cm^{-3})$	Carrier Mobility $(cm^2/V \cdot s)$
ZnOX	4.46	- 4.48	2.57
ZnO:Sb00	2.60	- 2.94	3.46
ZnO:Sb01	0.19	- 12.57	1.22
ZnO:Sb03	0.08	- 23.10	1.41
ZnO:Sb05	0.09	- 53.25	1.39
ZnO:Sb07	0.13	- 49.28	1.30
ZnO:Sb09	0.11	- 20.00	1.79
ZnO:Sb11	0.11	- 15.87	1.91
ZnO:Sb13	0.18	- 104.08	0.83
ZnO:Sb15	0.16	- 43.32	0.92
ZnO:Sb17	0.22	- 13.30	1.33
ZnO:Sb19	0.20	- 13.53	1.07
ZnO:Sb21	0.28	- 32.70	0.58

6.3 Optical properties

As previously mentioned, a study on the optical transmittance and reflectance of each sample was performed between 300 and 900 nm. Then an average value between 400 and 700 nm for each measure was calculated and these values are summarised in Table 8 and plotted in Figure 14. The results show that the increase in Sb-doping, caused by the higher current applied, generates a slight decrease in the average transmittance, but the lowest value remains higher than 80%, so all samples have good optical transparency. As for reflectance, there's no relevant change in its value as it seems that it is independent of the doping level, at least for the samples studied.

Furthermore, as it is possible to observe in the transmittance and reflectance spectra in Figure 15, the lines tend to overlap with no significant differences, which, simply put, means there's not a big alteration in both spectrums, except for the ZnO:Sb01 sample. When it comes to transparency, from 400

nm to 900 nm the films all have large values and, added to the non-alteration of the spectrum, the films keep the natural good transparency of ZnO in the Vis and UV, independently of doping level.

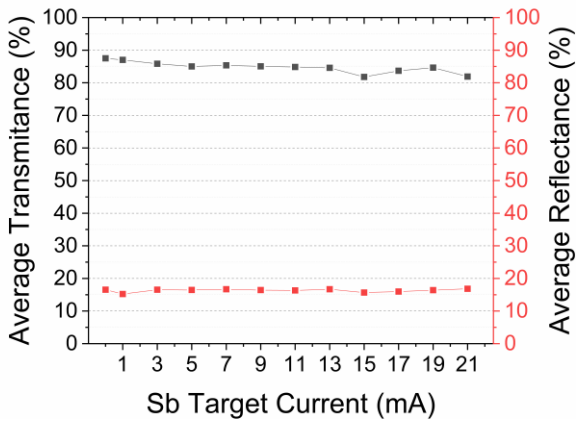

Figure 14: Average transmittance and reflectance as function of the current applied on the Sb target.

Table 8: Optical properties of each sample, namely transmittance and reflectance.

Sample	Average Transmittance (%)	Average Reflectance (%)
ZnOX	87.41	16.74
ZnO:Sb00	87.50	16.54
ZnO:Sb01	87.01	15.21
ZnO:Sb03	85.83	16.54
ZnO:Sb05	85.00	16.45
ZnO:Sb07	85.35	16.69
ZnO:Sb09	85.03	16.42
ZnO:Sb11	84.83	16.33
ZnO:Sb13	84.59	16.69
ZnO:Sb15	81.80	15.65
ZnO:Sb17	83.69	15.99
ZnO:Sb19	84.66	16.39
ZnO:Sb21	81.91	15.93

*Average transmittance and reflectance calculated between 400 and 700 nm.

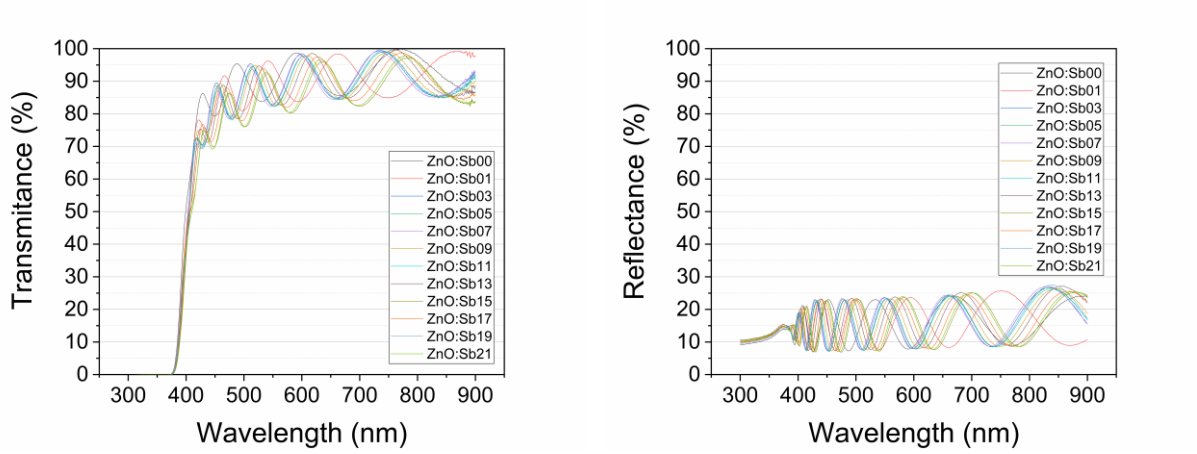

Figure 15: (a) Optical transmittance spectra of each sample, (b) Optical reflectance spectra of each sample.

6.4 Thermoelectric results

The Seebeck coefficient of each film was measured in a custom-made setup and it presented interesting values. As expected, the control sample and the ZnO:Sb00 sample have significantly low values, - 2.8 and - 6.5 $\mu V \cdot K^{-1}$ respectively, but the Seebeck coefficient quickly rises for the other films, with small exceptions. In most cases it reached absolute values close to 100 $\mu V \cdot K^{-1}$, in module, with the highest of 100.4 $\mu V \cdot K^{-1}$ corresponding to the ZnO:Sb13. As is observable in Figure 16 (a), the Seebeck coefficient stabilizes for higher currents. Furthermore, its negative nature corroborates what was previously concluded, that the films display n-type conductivity. When associated with electrical conductivity, the films showcased interesting values for PF, with the highest being 1.1 $mW \cdot m^{-1} \cdot K^{-2}$, which is much higher than all the values found in the literature. As expected, the highest PF value corresponds to the sample with the highest absolute Seebeck coefficient (ZnO:Sb13), but this sample also showed the highest absolute value for carrier concentration, and this and other beneficial electrical properties, such as resistivity, also influenced the PF value of the sample, making it the most successful film fabricated and the best example of the positive effect of Sb-doping in terms of TE performance.

Finalizing and considering all the properties previously mentioned, several films with good characteristics were developed and the results fundament the potential for ZnO:Sb thin films in practical applications.

In a more general sense, all thin films have a thickness under 800 nm and retain the good inherent optical properties of ZnO, preserving transparency, with an average transmittance of over 80 % for all samples. Therefore, optically transparent TE thin films were successfully fabricated.

Table 9: Seebeck coefficient measured with a custom-made system, electrical conductivity calculated from the resistivity measured with the Hall effect and the resulting PF.

Sample	Seebeck coefficient $(\mu V/K)$	Electrical Conductivity $(\Omega^{-1} \cdot cm^{-1})$	Power Factor $(mW \cdot m^{-1} \cdot K^{-2})$
ZnOX	- 2.8	0.22	0.2×10^{-4}
ZnO:Sb00	- 6.5	0.39	0.2×10^{-3}
ZnO:Sb01	- 27.1	5.18	0.4×10^{-2}
ZnO:Sb03	- 95.9	12.20	1.1
ZnO:Sb05	- 69.2	10.60	0.5
ZnO:Sb07	- 74.7	7.61	0.4
ZnO:Sb09	- 93.0	9.29	0.8
ZnO:Sb11	- 74.4	8.96	0.5
ZnO:Sb13	- 100.4	5.43	0.5
ZnO:Sb15	- 96.2	6.12	0.6
ZnO:Sb17	- 94.5	4.62	0.4
ZnO:Sb19	- 86.1	4.93	0.4
ZnO:Sb21	- 96.9	3.53	0.3

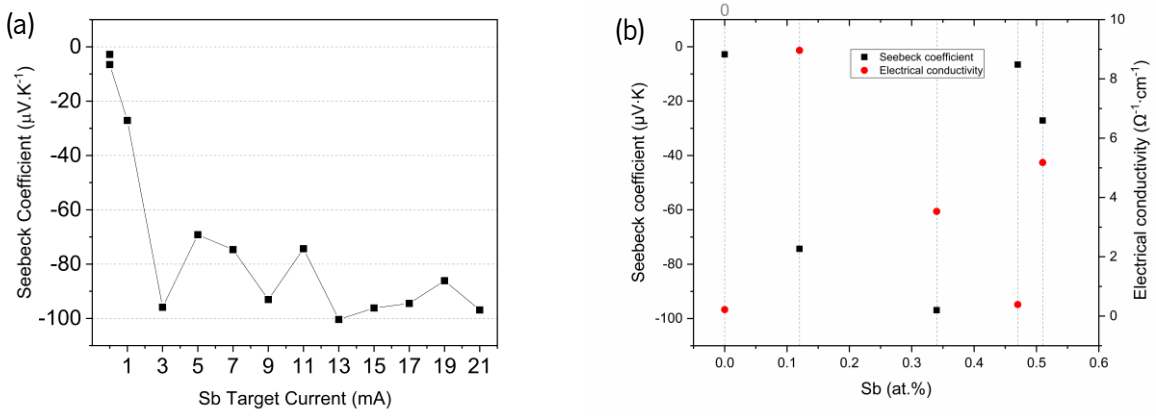

Figure 16: (a) Seebeck coefficient as function of the current applied in the Sb target. (b) Seebeck coefficient and electrical conductivity as functions of the Sb content.

Table 10: Samples and respective important properties, Seebeck coefficient in module |S|, electrical resistivity (ρ), carrier concentration (n), carrier mobility (μ), mean and quadratic roughness (Ra, Rq), thickness calculated and measured by SEM analysis (t (SEM)), Sb content, average transmittance and reflectance ($\overline{T}, \overline{R}$) and energy band gap (Eg).

Sample	$\|S\|$ $(\mu V/K)$	ρ $(\Omega \cdot cm)$	n $(\times 10^{18} cm^{-3})$	μ $(cm^2/V \cdot s)$	**Ra** (nm)	**Rq** (nm)	**t (SEM)** (nm)	**Sb** (at.%)	$\overline{T}$ (%)	$\overline{R}$ (%)	**Eg** (eV)
ZnOX	2.8	4.46	- 4.48	2.57	4.97	6.35	578.47	-	87.41	16.74	3.26
ZnO:Sb00	6.5	2.60	- 2.94	3.46	-	-	627.03	0.47	87.50	16.54	3.26
ZnO:Sb01	27.1	0.19	- 12.57	1.22	4.82	6.35	702.30	0.51	87.01	15.21	3.25
ZnO:Sb03	95.9	0.08	- 23.10	1.41	9.52	11.84	719.01	-	85.83	16.54	3.25
ZnO:Sb05	69.2	0.09	- 53.25	1.39	-	-	740.74	-	85.00	16.45	3.25
ZnO:Sb07	74.7	0.13	- 49.28	1.30	5.23	6.59	757.60	-	85.35	16.69	3.24
ZnO:Sb09	93.0	0.11	- 20.00	1.79	-	-	771.38	-	85.03	16.42	3.26
ZnO:Sb11	74.4	0.11	- 15.87	1.91	-	-	778.07	0.12	84.83	16.33	3.25
ZnO:Sb13	100.4	0.18	- 104.08	0.83	8.93	11.21	782.57	-	84.59	16.69	3.25
ZnO:Sb15	96.2	0.16	- 43.32	0.92	-	-	785.20	-	81.80	15.65	3.24
ZnO:Sb17	94.5	0.22	- 13.30	1.33	-	-	787.07	-	83.69	15.99	3.25
ZnO:Sb19	86.1	0.20	- 13.53	1.07	-	-	788.52	-	84.66	16.39	3.25
ZnO:Sb21	96.9	0.28	- 32.70	0.58	9.84	12.10	789.70	0.34	81.91	15.93	3.24

7. CONCLUSIONS

The goal of this paper was to perform a full study on the effects of Sb-doping in optically transparent ZnO thin films to evaluate the relevance of this material for TE applications, more specifically TCO technology. Several samples were fabricated with variating deposition parameters, namely the induced current in the doping target of Sb, to study the effect of this dopant on the film properties and, additionally, to understand the effect of the inducing current in the deposition.

For the study of these thin films, several techniques were used according to the desired properties: an extensive Hall effect study was performed to obtain the electrical properties; optical properties, more specifically transmittance and reflectance, were measured; film thickness was verified with SEM analysis and calculations with the transmittance spectra; surface morphology was studied with AFM analysis; film composition was analysed with XPS and EDX analysis; XRD analysis was performed to study the crystallographic structure of the thin films; and lastly the Seebeck coefficient was measured, and the PF calculated.

The thin films produced ranged in thickness between 600 and 800 nm and shared an energy band gap of 3.25 eV, without relevant variations, and high transmittance, above 80 %. Unfortunately, the composition study was limited and the results were not the ones anticipated. Before the depositions, it was expected that the Sb content would increase alongside the induced current in the Sb target, but this was not verified. This could have happened due to errors in measurements or deposition, but more tests would be needed for clearer results. Nevertheless, the presence of Sb was verified, even though in low quantities, and its effect on the films' properties was prevalent. The doped thin films showed significantly lower electrical resistivity values, with the lowest being 0.08 Ω·cm, and higher carrier concentrations, with an highest absolute value of 104.08×10^{18} cm^{-3}, which leads to conclude that the produced films were significantly enhanced in electrical conductivity because of the presence of Sb. Additionally, since the Sb content was low, not surpassing 0.51 at.% in the EDX analysis and only showing 1.0 at.% in the XPS analysis, and it still had a relatively high effect on the conducting properties of the samples, it's reasonable to assume that, if it's possible to increase doping and Sb content level, it's plausible to expect even better results for the electrical conductivity of the film. Furthermore, the films achieved excellent TE performance reaching the highest absolute Seebeck coefficient of 100 $\mu V \cdot K^{-1}$, in module and a respective PF with an

impressing value of 1.1 $mW \cdot m^{-1} \cdot K^{2}$. Once again, these values were obtained with low Sb content, so this doping process has the potential for better results. Two of the three conditions for the production of a good TE material were fulfilled, respectively, enhancing electrical conductivity and improving the Seebeck coefficient. The one missing is the enhancement of the thermal conductivity, which, with higher roughness values for the doped films, might've taken place but, without testing, couldn't be verified by this study. Moreover, the optical transparency remained with the doping so it was proven that Sb-doping of ZnO is a good and promising solution to TCO-based applications.

8. FUTURE WORK

Although this study helped show the potential for ZnO:Sb thin films in TE technology and TCO applications, there is still much more to be done. More studies on the effect of Sb content must be performed, with a proper focus on the integration of the Sb particles in the film. Additionally, these studies must take into account the thermal conductivity, which lacked in this case. Without considering all the thermoelectrical, optical and electrical properties it's impossible to discover the optimal deposition techniques for this material and its viability as a TE material. Furthermore, it's possible to achieve ZnO p-type doping with Sb, but the research around this is still lacking.

When the fundamental properties of the material are well understood, it would be interesting to test its performance in practical applications. A good approach would be to search for good substrates and create a TE generator or test nanostructures, which tend to show very good results in TE applications. With appealing results, it would be possible to implement those applications in electronic devices and, perhaps one day, use this material in display screens and windows of skyscrapers for thermal heat harvesting, positively contributing to solving the global energy emerging problem.

BIBLIOGRAPHY

[1] US Energy Information Administration, IEO 2021 Narrative, n.d. www.eia.gov (accessed January 19, 2023).

[2] International Energy Agency, World Energy Outlook 2021, 2021. www.iea.org/weo (accessed January 19, 2023).

[3] H. Jouhara, N. Khordehgah, S. Almahmoud, B. Delpech, A. Chauhan, S.A. Tassou, Waste heat recovery technologies and applications, Thermal Science and Engineering Progress. 6 (2018) 268–289. https://doi.org/10.1016/j.tsep.2018.04.017.

[4] J.M. Cullen, J.M. Allwood, Theoretical efficiency limits for energy conversion devices, Energy. 35 (2010) 2059–2069. https://doi.org/10.1016/j.energy.2010.01.024.

[5] Reducing energy costs with economisers improve operating efficiency, (n.d.). https://thermtech.co.uk/reducing-energy-costs-with-economisers/ (accessed January 19, 2023).

[6] R. Nicholson, Recuperative and regenerative techniques at high temperature, Journal of Heat Recovery Systems. 3 (1983) 385–404. https://doi.org/10.1016/0198-7593(83)90053-X.

[7] B. Varghese, D. Das, D. Devassy, S.G. K, A. Professor, U. Graduate Students, Design and Cost Optimization of Plate Heat Exchanger, 2014. www.researchinventy.com.

[8] A. Faghri, Heat pipes: review, opportunities and challenges, Frontiers in Heat Pipes. 5 (2014). https://doi.org/10.5098/fhp.5.1.

[9] Heat Pump Systems | Department of Energy, (n.d.). https://www.energy.gov/energysaver/heat-pump-systems (accessed January 19, 2023).

[10] H.A. Gabbar, Y. Koraz, Safety design of resilient micro energy grids, in: Smart Energy Grid Engineering, Elsevier, 2017: pp. 101–149. https://doi.org/10.1016/B978-0-12-805343-0.00005-X.

[11] H. Elahi, M. Eugeni, P. Gaudenzi, A Review on Mechanisms for Piezoelectric-Based Energy Harvesters, Energies (Basel). 11 (2018) 1850. https://doi.org/10.3390/en11071850.

[12] Y.K. Ramadass, A.P. Chandrakasan, An Efficient Piezoelectric Energy Harvesting Interface Circuit Using a Bias-Flip Rectifier and Shared Inductor, IEEE J Solid-State Circuits. 45 (2010) 189–204. https://doi.org/10.1109/JSSC.2009.2034442.

[13] P. Gambier, S.R. Anton, N. Kong, A. Erturk, D.J. Inman, Piezoelectric, solar and thermal energy harvesting for hybrid low-power generator systems with thin-film batteries, Meas Sci Technol. 23 (2012) 015101. https://doi.org/10.1088/0957-0233/23/1/015101.

[14] T. Hendricks, W.T. Choate, Engineering Scoping Study of Thermoelectric Generator Systems for Industrial Waste Heat Recovery, 2006. https://doi.org/10.2172/1218711.

[15] X. Sun, An Overview on Piezoelectric Power Generation System for Electricity Generation, Journal of Power and Energy Engineering. 05 (2017) 11–18. https://doi.org/10.4236/jpee.2017.52002.

[16] M.A. Cayless, Thermionic generation of electricity, British Journal of Applied Physics. 12 (1961) 433–442. https://doi.org/10.1088/0508-3443/12/9/303.

[17] K.A. Abdul Khalid, T.J. Leong, K. Mohamed, Review on Thermionic Energy Converters, IEEE Trans Electron Devices. 63 (2016) 2231–2241. https://doi.org/10.1109/TED.2016.2556751.

[18] V. v. Viswanathan, R.W. Davies, J.D. Holbery, Opportunity Analysis for Recovering Energy from Industrial Waste Heat and Emissions, Richland, WA (United States), 2006. https://doi.org/10.2172/1012899.

[19] M. Bianchi, C. Ferrari, F. Melino, A. Peretto, Feasibility study of a Thermo-Photo-Voltaic system for CHP application in residential buildings, Appl Energy. 97 (2012) 704–713. https://doi.org/10.1016/j.apenergy.2012.01.049.

[20] G. Attolini, M. Bosi, C. Ferrari, F. Melino, Design guidelines for thermo-photo-voltaic generator: The critical role of the emitter size, Appl Energy. 103 (2013) 618–626. https://doi.org/10.1016/j.apenergy.2012.10.032.

[21] F. Bouzid, L. Dehimi, Performance evaluation of a GaSb thermophotovoltaic converter, Journal of Renewable Energies. 15 (2012) 383–397.

[22] J. van der Heide, N.E. Posthuma, G. Flamand, W. Geens, J. Poortmans, Cost-efficient thermophotovoltaic cells based on germanium substrates, Solar Energy Materials and Solar Cells. 93 (2009) 1810–1816. https://doi.org/10.1016/j.solmat.2009.06.017.

[23] S. LeBlanc, Thermoelectric generators: Linking material properties and systems engineering for waste heat recovery applications, Sustainable Materials and Technologies. 1–2 (2014) 26–35. https://doi.org/10.1016/j.susmat.2014.11.002.

[24] K. Yazawa, A. Shakouri, Thermal optimization of embedded thermoelectric generators in refractory furnaces, in: 2016 15th IEEE Intersociety Conference on Thermal and Thermomechanical

Phenomena in Electronic Systems (ITherm), IEEE, 2016: pp. 1489–1493. https://doi.org/10.1109/ITHERM.2016.7517724.

[25] Duck Young Chung, T. Hogan, J. Schindler, L. Iordarridis, P. Brazis, C.R. Kannewurf, Baoxing Chen, C. Uher, M.G. Kanatzidis, Complex bismuth chalcogenides as thermoelectrics, in: XVI ICT '97. Proceedings ICT'97. 16th International Conference on Thermoelectrics (Cat. No.97TH8291), IEEE, 1997: pp. 459–462. https://doi.org/10.1109/ICT.1997.667185.

[26] R. Venkatasubramanian, E. Siivola, T. Colpitts, B. O'Quinn, Thin-film thermoelectric devices with high room-temperature figures of merit, Nature. 413 (2001) 597–602. https://doi.org/10.1038/35098012.

[27] J.P. Heremans, V. Jovovic, E.S. Toberer, A. Saramat, K. Kurosaki, A. Charoenphakdee, S. Yamanaka, G.J. Snyder, Enhancement of Thermoelectric Efficiency in PbTe by Distortion of the Electronic Density of States, Science (1979). 321 (2008) 554–557. https://doi.org/10.1126/science.1159725.

[28] Y. Pei, A. LaLonde, S. Iwanaga, G.J. Snyder, High thermoelectric figure of merit in heavy hole dominated PbTe, Energy Environ Sci. 4 (2011) 2085. https://doi.org/10.1039/c0ee00456a.

[29] Y. Pei, X. Shi, A. LaLonde, H. Wang, L. Chen, G.J. Snyder, Convergence of electronic bands for high performance bulk thermoelectrics, Nature. 473 (2011) 66–69. https://doi.org/10.1038/nature09996.

[30] A. Kandemir, A. Ozden, T. Cagin, C. Sevik, Thermal conductivity engineering of bulk and one-dimensional Si-Ge nanoarchitectures, Sci Technol Adv Mater. 18 (2017) 187–196. https://doi.org/10.1080/14686996.2017.1288065.

[31] A.U. Khan, N. Vlachos, Th. Kyratsi, High thermoelectric figure of merit of Mg2Si0.55Sn0.4Ge0.05 materials doped with Bi and Sb, Scr Mater. 69 (2013) 606–609. https://doi.org/10.1016/j.scriptamat.2013.07.008.

[32] G.S. Nolas, G.A. Slack, D.T. Morelli, T.M. Tritt, A.C. Ehrlich, The effect of rare-earth filling on the lattice thermal conductivity of skutterudites, J Appl Phys. 79 (1996) 4002. https://doi.org/10.1063/1.361828.

[33] K. Safeen, V. Micheli, R. Bartali, G. Gottardi, A. Safeen, H. Ullah, N. Laidani, Influence of intrinsic defects on the electrical and optical properties of TiO2:Nb films sputtered at room temperature, Thin Solid Films. 645 (2018) 173–179. https://doi.org/10.1016/j.tsf.2017.10.028.

[34] J. Tao, H. Pan, L.M. Wong, T.I. Wong, J.W. Chai, J. Pan, S.J. Wang, Mechanism of insulator-to-metal transition in heavily Nb doped anatase TiO_2, Mater Res Express. 1 (2014) 015911. https://doi.org/10.1088/2053-1591/1/1/015911.

[35] T. Minami, Transparent conducting oxide semiconductors for transparent electrodes, Semicond Sci Technol. 20 (2005) S35–S44. https://doi.org/10.1088/0268-1242/20/4/004.

[36] Transparent Conductive Films (TCF) 2017-2027: Forecasts, Markets, Technologies: IDTechEx, (n.d.). https://www.idtechex.com/en/research-report/transparent-conductive-films-tcf-2017-2027-forecasts-markets-technologies/524 (accessed January 19, 2023).

[37] Thermoelectric Energy Harvesting 2018-2028: Applications, Markets, Players: IDTechEx, (n.d.). https://www.idtechex.com/fr/research-report/thermoelectric-energy-harvesting-2018-2028-applications-markets-players/582 (accessed January 19, 2023).

[38] K.B. Spooner, A.M. Ganose, D.O. Scanlon, Assessing the limitations of transparent conducting oxides as thermoelectrics, J Mater Chem A Mater. 8 (2020) 11948–11957. https://doi.org/10.1039/D0TA02247K.

[39] L.C. Ding, A. Akbarzadeh, L. Tan, A review of power generation with thermoelectric system and its alternative with solar ponds, Renewable and Sustainable Energy Reviews. 81 (2018) 799–812. https://doi.org/10.1016/j.rser.2017.08.010.

[40] B.M. Morais Faustino, D. Gomes, J. Faria, T. Juntunen, G. Gaspar, C. Bianchi, A. Almeida, A. Marques, I. Tittonen, I. Ferreira, CuI p-type thin films for highly transparent thermoelectric p-n modules, Sci Rep. 8 (2018) 6867. https://doi.org/10.1038/s41598-018-25106-3.

[41] D. Beretta, N. Neophytou, J.M. Hodges, M.G. Kanatzidis, D. Narducci, M. Martin- Gonzalez, M. Beekman, B. Balke, G. Cerretti, W. Tremel, A. Zevalkink, A.I. Hofmann, C. Müller, B. Dörling, M. Campoy-Quiles, M. Caironi, Thermoelectrics: From history, a window to the future, Materials Science and Engineering: R: Reports. 138 (2019) 100501. https://doi.org/10.1016/j.mser.2018.09.001.

[42] R.P. CHASMAR, R. STRATTON, The Thermoelectric Figure of Merit and its Relation to Thermoelectric Generators†, Journal of Electronics and Control. 7 (1959) 52–72. https://doi.org/10.1080/00207215908937186.

[43] S.M. Rossnagel, Thin film deposition with physical vapor deposition and related technologies, Journal of Vacuum Science & Technology A: Vacuum, Surfaces, and Films. 21 (2003) S74–S87. https://doi.org/10.1116/1.1600450.

[44] T.M. Tritt, M.A. Subramanian, Thermoelectric Materials, Phenomena, and Applications: A Bird's Eye View, MRS Bull. 31 (2006) 188–198. https://doi.org/10.1557/mrs2006.44.

[45] Thin Film Materials Selection Guide: Types, Features, Applications | Engineering360, (n.d.). https://www.globalspec.com/learnmore/materials_chemicals_adhesives/electrical_optical_specialty_materials/thin_film_materials (accessed January 19, 2023).

[46] M.S. Dresselhaus, G. Chen, M.Y. Tang, R.G. Yang, H. Lee, D.Z. Wang, Z.F. Ren, J. -P. Fleurial, P. Gogna, New Directions for Low-Dimensional Thermoelectric Materials, Advanced Materials. 19 (2007) 1043–1053. https://doi.org/10.1002/adma.200600527.

[47] Q. Zhang, X. Ai, L. Wang, Y. Chang, W. Luo, W. Jiang, L. Chen, Improved Thermoelectric Performance of Silver Nanoparticles-Dispersed Bi_2Te_3 Composites Deriving from Hierarchical Two-Phased Heterostructure, Adv Funct Mater. 25 (2015) 966–976. https://doi.org/10.1002/adfm.201402663.

[48] Y. Zhou, L. Li, Q. Tan, J.-F. Li, Thermoelectric properties of Pb-doped bismuth telluride thin films deposited by magnetron sputtering, J Alloys Compd. 590 (2014) 362–367. https://doi.org/10.1016/j.jallcom.2013.12.136.

[49] P. Nuthongkum, R. Sakdanuphab, M. Horprathum, A. Sakulkalavek, [Bi]:[Te] Control, Structural and Thermoelectric Properties of Flexible Bi x Te y Thin Films Prepared by RF Magnetron Sputtering at Different Sputtering Pressures, J Electron Mater. 46 (2017) 6444–6450. https://doi.org/10.1007/s11664-017-5671-x.

[50] R. Nunna, P. Qiu, M. Yin, H. Chen, R. Hanus, Q. Song, T. Zhang, M.-Y. Chou, M.T. Agne, J. He, G.J. Snyder, X. Shi, L. Chen, Ultrahigh thermoelectric performance in Cu2Se-based hybrid materials with highly dispersed molecular CNTs, Energy Environ Sci. 10 (2017) 1928–1935. https://doi.org/10.1039/C7EE01737E.

[51] Z. Lin, C. Hollar, J.S. Kang, A. Yin, Y. Wang, H. Shiu, Y. Huang, Y. Hu, Y. Zhang, X. Duan, A Solution Processable High-Performance Thermoelectric Copper Selenide Thin Film, Advanced Materials. 29 (2017) 1606662. https://doi.org/10.1002/adma.201606662.

[52] C. Yang, D. Souchay, M. Kneiß, M. Bogner, H.M. Wei, M. Lorenz, O. Oeckler, G. Benstetter, Y.Q. Fu, M. Grundmann, Transparent flexible thermoelectric material based on non-toxic earth-abundant p-type copper iodide thin film, Nat Commun. 8 (2017) 16076. https://doi.org/10.1038/ncomms16076.

[53] I. Terasaki, Y. Sasago, K. Uchinokura, Large thermoelectric power in NaCo2O4 single crystals, Phys Rev B. 56 (1997) R12685–R12687. https://doi.org/10.1103/PhysRevB.56.R12685.

[54] A.C. Masset, C. Michel, A. Maignan, M. Hervieu, O. Toulemonde, F. Studer, B. Raveau, J. Hejtmanek, Misfit-layered cobaltite with an anisotropic giant magnetoresistance: Ca3Co4O9, Phys Rev B. 62 (2000) 166–175. https://doi.org/10.1103/PhysRevB.62.166.

[55] B. Paul, J. Lu, P. Eklund, Nanostructural Tailoring to Induce Flexibility in Thermoelectric $Ca_3Co_4O_9$ Thin Films, ACS Appl Mater Interfaces. 9 (2017) 25308–25316. https://doi.org/10.1021/acsami.7b06301.

[56] B. Paul, E.M. Björk, A. Kumar, J. Lu, P. Eklund, Nanoporous Ca3Co4O9 Thin Films for Transferable Thermoelectrics, ACS Appl Energy Mater. 1 (2018) 2261–2268. https://doi.org/10.1021/acsaem.8b00333.

[57] G.B. Bronner, S.A. Cohen, D.M. Dobuzinsky, J.P. Gambino, H.L. Ho, K.P. Madden, High dielectric TiO2-SiN composite films for memory applications, 1999.

[58] K.F. Albertin, M.A. Valle, I. Pereyra, Study Of MOS Capacitors With TiO2 And SiO2/TiO2 Gate Dielectric, Journal of Integrated Circuits and Systems. 2 (2007) 89–93. https://doi.org/10.29292/jics.v2i2.272.

[59] J.M. Ribeiro, F.C. Correia, F.J. Rodrigues, J.S. Reparaz, A.R. Goñi, C.J. Tavares, Transparent niobium-doped titanium dioxide thin films with high Seebeck coefficient for thermoelectric applications, Surf Coat Technol. 425 (2021) 127724. https://doi.org/10.1016/j.surfcoat.2021.127724.

[60] J.M. Ribeiro, F.C. Correia, A. Kuzmin, I. Jonane, M. Kong, A.R. Goñi, J.S. Reparaz, A. Kalinko, E. Welter, C.J. Tavares, Influence of Nb-doping on the local structure and thermoelectric properties of transparent TiO2:Nb thin films, J Alloys Compd. 838 (2020) 155561. https://doi.org/10.1016/j.jallcom.2020.155561.

[61] I. Lévesque, P.-O. Bertrand, N. Blouin, M. Leclerc, S. Zecchin, G. Zotti, C.I. Ratcliffe, D.D. Klug, X. Gao, F. Gao, J.S. Tse, Synthesis and Thermoelectric Properties of Polycarbazole, Polyindolocarbazole, and Polydiindolocarbazole Derivatives, Chemistry of Materials. 19 (2007) 2128–2138. https://doi.org/10.1021/cm070063h.

[62] O. Bubnova, X. Crispin, Towards polymer-based organic thermoelectric generators, Energy Environ Sci. 5 (2012) 9345. https://doi.org/10.1039/c2ee22777k.

[63] R. Zuzok, A.B. Kaiser, W. Pukacki, S. Roth, Thermoelectric power and conductivity of iodine-doped ‘“new”’ polyacetylene, J Chem Phys. 95 (1991) 1270–1275. https://doi.org/10.1063/1.461107.

[64] Y.W. Park, C.O. Yoon, B.C. Na, H. Shirakawa, K. Akagi, Metallic properties of transition metal halides doped polyacetylene: The soliton liquid state, Synth Met. 41 (1991) 27–32. https://doi.org/10.1016/0379-6779(91)90989-I.

[65] Y. Sun, Z. Wei, W. Xu, D. Zhu, A three-in-one improvement in thermoelectric properties of polyaniline brought by nanostructures, Synth Met. 160 (2010) 2371–2376. https://doi.org/10.1016/j.synthmet.2010.09.014.

[66] J. Li, X. Tang, H. Li, Y. Yan, Q. Zhang, Synthesis and thermoelectric properties of hydrochloric acid-doped polyaniline, Synth Met. 160 (2010) 1153–1158. https://doi.org/10.1016/j.synthmet.2010.03.001.

[67] E.R. Holland, S.J. Pomfret, P.N. Adams, L. Abell, A.P. Monkman, Doping dependent transport properties of polyaniline-CSA films, Synth Met. 84 (1997) 777–778. https://doi.org/10.1016/S0379-6779(96)04141-0.

[68] N.T. Kemp, A.B. Kaiser, C.-J. Liu, B. Chapman, O. Mercier, A.M. Carr, H.J. Trodahl, R.G. Buckley, A.C. Partridge, J.Y. Lee, C.Y. Kim, A. Bartl, L. Dunsch, W.T. Smith, J.S. Shapiro, Thermoelectric power and conductivity of different types of polypyrrole, J Polym Sci B Polym Phys. 37 (1999) 953–960. https://doi.org/10.1002/(SICI)1099-0488(19990501)37:9<953::AID-POLB7>3.0.CO;2-L.

[69] M. Culebras, B. Uriol, C.M. Gómez, A. Cantarero, Controlling the thermoelectric properties of polymers: application to PEDOT and polypyrrole, Physical Chemistry Chemical Physics. 17 (2015) 15140–15145. https://doi.org/10.1039/C5CP01940K.

[70] L. Bao-Yang, L. Cong-Cong, L. Shan, X. Jing-Kun, J. Feng-Xing, L. Yu-Zhen, Z. Zhuo, Thermoelectric Performances of Free-Standing Polythiophene and Poly(3-Methylthiophene) Nanofilms, Chinese Physics Letters. 27 (2010) 057201. https://doi.org/10.1088/0256-307X/27/5/057201.

[71] Y. Du, S.Z. Shen, K. Cai, P.S. Casey, Research progress on polymer–inorganic thermoelectric nanocomposite materials, Prog Polym Sci. 37 (2012) 820–841. https://doi.org/10.1016/j.progpolymsci.2011.11.003.

[72] Metal Organic Frameworks (MOFs), (n.d.). https://www.sigmaaldrich.com/PT/en/technical-documents/technical-article/materials-science-and-engineering/photovoltaics-and-solar-cells/metal-organic-frameworks (accessed January 19, 2023).

[73] K. Vikrant, V. Kumar, K.-H. Kim, D. Kukkar, Metal–organic frameworks (MOFs): potential and challenges for capture and abatement of ammonia, J Mater Chem A Mater. 5 (2017) 22877–22896. https://doi.org/10.1039/C7TA07847A.

[74] L. Sun, T. Miyakai, S. Seki, M. Dincă, Mn(2,5-disulfhydrylbenzene-1,4-dicarboxylate): A Microporous Metal–Organic Framework with Infinite (–Mn–S–) Chains and High Intrinsic Charge Mobility, J Am Chem Soc. 135 (2013) 8185–8188. https://doi.org/10.1021/ja4037516.

[75] K.J. Erickson, F. Léonard, V. Stavila, M.E. Foster, C.D. Spataru, R.E. Jones, B.M. Foley, P.E. Hopkins, M.D. Allendorf, A.A. Talin, Thin Film Thermoelectric Metal–Organic Framework with High Seebeck Coefficient and Low Thermal Conductivity, Advanced Materials. 27 (2015) 3453–3459. https://doi.org/10.1002/adma.201501078.

[76] C. Li, L. Zhang, J. Chen, X. Li, J. Sun, J. Zhu, X. Wang, Y. Fu, Recent development and applications of electrical conductive MOFs, Nanoscale. 13 (2021) 485–509. https://doi.org/10.1039/D0NR06396G.

[77] B. Olalde, J.M. Aizpurua, A. García, I. Bustero, I. Obieta, M.J. Jurado, Single-Walled Carbon Nanotubes and Multiwalled Carbon Nanotubes Functionalized with Poly(L-lactic acid): a Comparative Study, The Journal of Physical Chemistry C. 112 (2008) 10663–10667. https://doi.org/10.1021/jp800266j.

[78] Q. Yao, L. Chen, W. Zhang, S. Liufu, X. Chen, Enhanced Thermoelectric Performance of Single-Walled Carbon Nanotubes/Polyaniline Hybrid Nanocomposites, ACS Nano. 4 (2010) 2445–2451. https://doi.org/10.1021/nn1002562.

[79] C. Meng, C. Liu, S. Fan, A Promising Approach to Enhanced Thermoelectric Properties Using Carbon Nanotube Networks, Advanced Materials. 22 (2010) 535–539. https://doi.org/10.1002/adma.200902221.

[80] W. Luo, Y. Wang, L. Wang, W. Jiang, S.-L. Chou, S.X. Dou, H.K. Liu, J. Yang, Silicon/Mesoporous Carbon/Crystalline TiO2 Nanoparticles for Highly Stable Lithium Storage, ACS Nano. 10 (2016) 10524–10532. https://doi.org/10.1021/acsnano.6b06517.

[81] W. Luo, X. Chen, Y. Xia, M. Chen, L. Wang, Q. Wang, W. Li, J. Yang, Surface and Interface Engineering of Silicon-Based Anode Materials for Lithium-Ion Batteries, Adv Energy Mater. 7 (2017) 1701083. https://doi.org/10.1002/aenm.201701083.

[82] W. Luo, D. Shen, R. Zhang, B. Zhang, Y. Wang, S.X. Dou, H.K. Liu, J. Yang, Germanium Nanograin Decoration on Carbon Shell: Boosting Lithium-Storage Properties of Silicon Nanoparticles, Adv Funct Mater. 26 (2016) 7800–7806. https://doi.org/10.1002/adfm.201603335.

[83] W. Zhou, Q. Fan, Q. Zhang, L. Cai, K. Li, X. Gu, F. Yang, N. Zhang, Y. Wang, H. Liu, W. Zhou, S. Xie, High-performance and compact-designed flexible thermoelectric modules enabled by a

reticulate carbon nanotube architecture, Nat Commun. 8 (2017) 14886. https://doi.org/10.1038/ncomms14886.

[84] L. Wang, Q. Yao, J. Xiao, K. Zeng, S. Qu, W. Shi, Q. Wang, L. Chen, Engineered Molecular Chain Ordering in Single-Walled Carbon Nanotubes/Polyaniline Composite Films for High-Performance Organic Thermoelectric Materials, Chem Asian J. 11 (2016) 1804–1810. https://doi.org/10.1002/asia.201600212.

[85] C.H. Johansson, J.O. Linde, Röntgenographische Bestimmung der Atomanordnung in den Mischkristallreihen Au-Cu und Pd-Cu, Ann Phys. 383 (1925) 439–460. https://doi.org/10.1002/andp.19253832104.

[86] L.D. Hicks, T.C. Harman, X. Sun, M.S. Dresselhaus, Experimental study of the effect of quantum-well structures on the thermoelectric figure of merit, Phys Rev B. 53 (1996) R10493–R10496. https://doi.org/10.1103/PhysRevB.53.R10493.

[87] T.C. Harman, D.L. Spears, M.P. Walsh, PbTe/Te superlattice structures with enhanced thermoelectric figures of merit, J Electron Mater. 28 (1999) L1–L5. https://doi.org/10.1007/s11664-999-0198-4.

[88] T.C. Harman, P.J. Taylor, D.L. Spears, M.P. Walsh, Thermoelectric quantum-dot superlattices with high ZT, J Electron Mater. 29 (2000) L1–L2. https://doi.org/10.1007/s11664-000-0117-1.

[89] T.C. Harman, M.P. Walsh, B.E. laforge, G.W. Turner, Nanostructured thermoelectric materials, J Electron Mater. 34 (2005) L19–L22. https://doi.org/10.1007/s11664-005-0083-8.

[90] C.J. Vineis, T.C. Harman, S.D. Calawa, M.P. Walsh, R.E. Reeder, R. Singh, A. Shakouri, Carrier concentration and temperature dependence of the electronic transport properties of epitaxial PbTe and PbTe/PbSe nanodot superlattices, Phys Rev B. 77 (2008) 235202. https://doi.org/10.1103/PhysRevB.77.235202.

[91] R. Venkatasubramanian, E. Siivola, T. Colpitts, B. O'Quinn, Thin-film thermoelectric devices with high room-temperature figures of merit, Nature. 413 (2001) 597–602. https://doi.org/10.1038/35098012.

[92] X.W. Wang, H. Lee, Y.C. Lan, G.H. Zhu, G. Joshi, D.Z. Wang, J. Yang, A.J. Muto, M.Y. Tang, J. Klatsky, S. Song, M.S. Dresselhaus, G. Chen, Z.F. Ren, Enhanced thermoelectric figure of merit in nanostructured n-type silicon germanium bulk alloy, Appl Phys Lett. 93 (2008) 193121. https://doi.org/10.1063/1.3027060.

[93] G. Joshi, H. Lee, Y. Lan, X. Wang, G. Zhu, D. Wang, R.W. Gould, D.C. Cuff, M.Y. Tang, M.S. Dresselhaus, G. Chen, Z. Ren, Enhanced Thermoelectric Figure-of-Merit in Nanostructured p-type

Silicon Germanium Bulk Alloys, Nano Lett. 8 (2008) 4670–4674. https://doi.org/10.1021/nl8026795.

[94] A. Khitun, Jianlin Liu, K.L. Wang, Thermal conductivity of Si/Ge quantum dot superlattices, in: 4th IEEE Conference on Nanotechnology, 2004., IEEE, 2004: pp. 20–22. https://doi.org/10.1109/NANO.2004.1392236.

[95] C.-K. Liu, C.-K. Yu, H.-C. Chien, S.-L. Kuo, C.-Y. Hsu, M.-J. Dai, G.-L. Luo, S.-C. Huang, M.-J. Huang, Thermal conductivity of Si/SiGe superlattice films, J Appl Phys. 104 (2008) 114301. https://doi.org/10.1063/1.3032602.

[96] A. Samarelli, L. Ferre Llin, S. Cecchi, J. Frigerio, T. Etzelstorfer, E. Müller, Y. Zhang, J.R. Watling, D. Chrastina, G. Isella, J. Stangl, J.P. Hague, J.M.R. Weaver, P. Dobson, D.J. Paul, The thermoelectric properties of Ge/SiGe modulation doped superlattices, J Appl Phys. 113 (2013) 233704. https://doi.org/10.1063/1.4811228.

[97] Z. Aksamija, I. Knezevic, Thermal conductivity of Si1−xGex/Si1−yGey superlattices: Competition between interfacial and internal scattering, Phys Rev B. 88 (2013) 155318. https://doi.org/10.1103/PhysRevB.88.155318.

[98] C. Zhou, B.-M. Nguyen, M. Razeghi, M. Grayson, Thermal Conductivity of InAs/GaSb Type II Superlattice, J Electron Mater. 41 (2012) 2322–2325. https://doi.org/10.1007/s11664-012-2146-y.

[99] Ü. Özgür, Ya.I. Alivov, C. Liu, A. Teke, M.A. Reshchikov, S. Doğan, V. Avrutin, S.-J. Cho, H. Morkoç, A comprehensive review of ZnO materials and devices, J Appl Phys. 98 (2005) 041301. https://doi.org/10.1063/1.1992666.

[100] H. Chen, Y. Liu, C. Xie, J. Wu, D. Zeng, Y. Liao, A comparative study on UV light activated porous TiO2 and ZnO film sensors for gas sensing at room temperature, Ceram Int. 38 (2012) 503–509. https://doi.org/10.1016/j.ceramint.2011.07.035.

[101] A. Janotti, C.G. van de Walle, Fundamentals of zinc oxide as a semiconductor, Reports on Progress in Physics. 72 (2009) 126501. https://doi.org/10.1088/0034-4885/72/12/126501.

[102] H. Wang, G. Qin, G. Li, Q. Wang, M. Hu, Low thermal conductivity of monolayer ZnO and its anomalous temperature dependence, Physical Chemistry Chemical Physics. 19 (2017) 12882–12889. https://doi.org/10.1039/C7CP00460E.

[103] A. Mang, K. Reimann, St. Rübenacke, Band gaps, crystal-field splitting, spin-orbit coupling, and exciton binding energies in ZnO under hydrostatic pressure, Solid State Commun. 94 (1995) 251–254. https://doi.org/10.1016/0038-1098(95)00054-2.

[104] M. Al-Fandi, R. Oweis, B.A. Albiss, T. AlZoubi, M.-A. Al-Akhras, H. Qutaish, H. Khwailah, S. Al-Hattami, E. Al-Shawwa, A prototype Ultraviolet Light Sensor based on ZnO Nanoparticles/Graphene Oxide Nanocomposite Using Low Temperature Hydrothermal Method, IOP Conf Ser Mater Sci Eng. 92 (2015) 012009. https://doi.org/10.1088/1757-899X/92/1/012009.

[105] D.M. Bagnall, Y.F. Chen, Z. Zhu, T. Yao, S. Koyama, M.Y. Shen, T. Goto, Optically pumped lasing of ZnO at room temperature, Appl Phys Lett. 70 (1997) 2230–2232. https://doi.org/10.1063/1.118824.

[106] D.C. Reynolds, D.C. Look, B. Jogai, Optically pumped ultraviolet lasing from ZnO, Solid State Commun. 99 (1996) 873–875. https://doi.org/10.1016/0038-1098(96)00340-7.

[107] T. Yamamoto, T. Shiosaki, A. Kawabata, Characterization of ZnO piezoelectric films prepared by rf planar-magnetron sputtering, J Appl Phys. 51 (1980) 3113–3120. https://doi.org/10.1063/1.328100.

[108] J. Molarius, J. Kaitila, T. Pensala, M. Ylilammi, Piezoelectric ZnO ®lms by r.f. sputtering, Journal of Materials Science: Materials in Electronics. 14 (2003) 431–435. https://doi.org/https://doi.org/10.1023/A:1023929524641.

[109] P. Sharma, Z. Guler, N. Jackson, Development and characterization of confocal sputtered piezoelectric zinc oxide thin film, Vacuum. 184 (2021) 109930. https://doi.org/10.1016/j.vacuum.2020.109930.

[110] E.S. Nour, O. Nur, M. Willander, Zinc oxide piezoelectric nano-generators for low frequency applications, Semicond Sci Technol. 32 (2017) 064005. https://doi.org/10.1088/1361-6641/aa6bde.

[111] J.B. Franklin, B. Zou, P. Petrov, D.W. McComb, M.P. Ryan, M.A. McLachlan, Optimised pulsed laser deposition of ZnO thin films on transparent conducting substrates, J Mater Chem. 21 (2011) 8178. https://doi.org/10.1039/c1jm10658a.

[112] K. Sakurai, M. Kanehiro, K. Nakahara, Tetsuhiro Tanabe, S. Fujita, S. Fujita, Effects of oxygen plasma condition on MBE growth of ZnO, J Cryst Growth. 209 (2000) 522–525. https://doi.org/10.1016/S0022-0248(99)00610-7.

[113] Ü. Özgür, V. Avrutin, H. Morkoç, Zinc Oxide Materials and Devices Grown by Molecular Beam Epitaxy, in: Molecular Beam Epitaxy, Elsevier, 2018: pp. 343–375. https://doi.org/10.1016/B978-0-12-812136-8.00016-5.

[114] T. Weckman, K. Laasonen, Atomic Layer Deposition of Zinc Oxide: Study on the Water Pulse Reactions from First-Principles, The Journal of Physical Chemistry C. 122 (2018) 7685–7694. https://doi.org/10.1021/acs.jpcc.7b11469.

[115] M.N. Kamalasanan, S. Chandra, Sol-gel synthesis of ZnO thin films, Thin Solid Films. 288 (1996) 112–115. https://doi.org/10.1016/S0040-6090(96)08864-5.

[116] F. Paraguay D., W. Estrada L., D.R. Acosta N., E. Andrade, M. Miki-Yoshida, Growth, structure and optical characterization of high quality ZnO thin films obtained by spray pyrolysis, Thin Solid Films. 350 (1999) 192–202. https://doi.org/10.1016/S0040-6090(99)00050-4.

[117] A. Hachigo, H. Nakahata, K. Higaki, S. Fujii, S. Shikata, Heteroepitaxial growth of ZnO films on diamond (111) plane by magnetron sputtering, Appl Phys Lett. 65 (1994) 2556–2558. https://doi.org/10.1063/1.112634.

[118] J.G.E. Gardeniers, Z.M. Rittersma, G.J. Burger , Preferred orientation and piezoelectricity in sputtered ZnO films, J Appl Phys. 83 (1998) 7844–7854. https://doi.org/10.1063/1.367959.

[119] S.K. Tiku, C.K. Lau, K.M. Lakin, Chemical vapor deposition of ZnO epitaxial films on sapphire, Appl Phys Lett. 36 (1980) 318–320. https://doi.org/10.1063/1.91477.

[120] M. Kasuga, M. Mochizuki, Orientation relationships of zinc oxide on sapphire in heteroepitaxial chemical vapor deposition, J Cryst Growth. 54 (1981) 185–194. https://doi.org/10.1016/0022-0248(81)90459-0.

[121] S. Ilican, K. Gorgun, S. Aksoy, Y. Caglar, M. Caglar, Fabrication of p-Si/n-ZnO:Al heterojunction diode and determination of electrical parameters, J Mol Struct. 1156 (2018) 675–683. https://doi.org/10.1016/j.molstruc.2017.11.121.

[122] M.V. Castro, M.F. Cerqueira, L. Rebouta, P. Alpuim, C.B. Garcia, G.L. Júnior, C.J. Tavares, Influence of hydrogen plasma thermal treatment on the properties of ZnO:Al thin films prepared by dc magnetron sputtering, Vacuum. 107 (2014) 145–154. https://doi.org/10.1016/j.vacuum.2014.04.022.

[123] J. Loureiro, N. Neves, R. Barros, T. Mateus, R. Santos, S. Filonovich, S. Reparaz, C.M. Sotomayor-Torres, F. Wyczisk, L. Divay, R. Martins, I. Ferreira, Transparent aluminium zinc oxide thin films with enhanced thermoelectric properties, J. Mater. Chem. A. 2 (2014) 6649–6655. https://doi.org/10.1039/C3TA15052F.

[124] P. Jood, R.J. Mehta, Y. Zhang, G. Peleckis, X. Wang, R.W. Siegel, T. Borca-Tasciuc, S.X. Dou, G. Ramanath, Al-Doped Zinc Oxide Nanocomposites with Enhanced Thermoelectric Properties, Nano Lett. 11 (2011) 4337–4342. https://doi.org/10.1021/nl202439h.

[125] P. Fan, Z. Zheng, Y. Li, Q. Lin, J. Luo, G. Liang, X. Cai, D. Zhang, F. Ye, Low-cost flexible thin film thermoelectric generator on zinc based thermoelectric materials, Appl Phys Lett. 106 (2015) 073901. https://doi.org/10.1063/1.4909531.

[126] B.M. Ataev, A.M. Bagamadova, A.M. Djabrailov, V.V. Mamedov, R.A. Rabadanov, Highly conductive and transparent Ga-doped epitaxial ZnO films on sapphire by CVD, Thin Solid Films. 260 (1995) 19–20. https://doi.org/10.1016/0040-6090(94)09485-3.

[127] X. Wang, X. Huang, Z.M. Wong, A. Suwardi, Y. Zheng, F. Wei, S. Wang, T.L. Tan, G. Wu, Q. Zhu, H. Tanoto, K.S. Ong, S.-W. Yang, A.Q. Yan, J. Xu, Gallium-Doped Zinc Oxide Nanostructures for Tunable Transparent Thermoelectric Films, ACS Appl Nano Mater. 5 (2022) 8631–8639. https://doi.org/10.1021/acsanm.2c02159.

[128] G. Singh, S.B. Shrivastava, D. Jain, S. Pandya, T. Shripathi, V. Ganesan, Effect of indium doping on zinc oxide films prepared by chemical spray pyrolysis technique, Bulletin of Materials Science. 33 (2010) 581–587. https://doi.org/10.1007/s12034-010-0089-6.

[129] C.H. Park, S.B. Zhang, S.-H. Wei, Origin of p-type doping difficulty in ZnO: The impurity perspective, Phys Rev B. 66 (2002) 073202. https://doi.org/10.1103/PhysRevB.66.073202.

[130] F.C. Correia, J.M. Ribeiro, A. Kuzmin, I. Pudza, A. Kalinko, E. Welter, A. Mendes, J. Rodrigues, N.B. Sedrine, T. Monteiro, M.R. Correia, C.J. Tavares, The role of Ga and Bi doping on the local structure of transparent zinc oxide thin films, J Alloys Compd. 870 (2021) 159489. https://doi.org/10.1016/j.jallcom.2021.159489.

[131] D.C. Look, D.C. Reynolds, C.W. Litton, R.L. Jones, D.B. Eason, G. Cantwell, Characterization of homoepitaxial p-type ZnO grown by molecular beam epitaxy, Appl Phys Lett. 81 (2002) 1830–1832. https://doi.org/10.1063/1.1504875.

[132] L. Li, C.X. Shan, B.H. Li, J.Y. Zhang, B. Yao, D.Z. Shen, X.W. Fan, Y.M. Lu, An approach to enhanced acceptor concentration in ZnO:N films, J Mater Sci. 45 (2010) 4093–4096. https://doi.org/10.1007/s10853-010-4497-1.

[133] M. Ding, D. Zhao, B. Yao, B. Li, Z. Zhang, D. Shen, The p-type ZnO film realized by a hydrothermal treatment method, Appl Phys Lett. 98 (2011) 062102. https://doi.org/10.1063/1.3549304.

[134] L.-C. Chao, J.-W. Chen, H.-C. Peng, C.-H. Ho, Characterization of nitrogen doped p-type ZnO thin films prepared by reactive ion beam sputter deposition, Surf Coat Technol. 231 (2013) 492–495. https://doi.org/10.1016/j.surfcoat.2012.10.077.

[135] D. Snigurenko, K. Kopalko, T.A. Krajewski, R. Jakiela, E. Guziewicz, Nitrogen doped p-type ZnO films and p-n homojunction, Semicond Sci Technol. 30 (2015) 015001. https://doi.org/10.1088/0268-1242/30/1/015001.

[136] T.K. Pathak, V. Kumar, H.C. Swart, L.P. Purohit, Effect of doping concentration on the conductivity and optical properties of p-type ZnO thin films, Physica B Condens Matter. 480 (2016) 31–35. https://doi.org/10.1016/j.physb.2015.09.033.

[137] Y.-P. Jin, B. Zhang, J.-Z. Wang, L.-Q. Shi, P-Type Nitrogen-Doped ZnO Films Prepared by In-Situ Thermal Oxidation of Zn3N2 Films, Chinese Physics Letters. 33 (2016) 058101. https://doi.org/10.1088/0256-307X/33/5/058101.

[138] K. Tang, S.-L. Gu, J.-D. Ye, S.-M. Zhu, R. Zhang, Y.-D. Zheng, Recent progress of the native defects and p-type doping of zinc oxide, Chinese Physics B. 26 (2017) 047702. https://doi.org/10.1088/1674-1056/26/4/047702.

[139] F.X. Xiu, Z. Yang, L.J. Mandalapu, D.T. Zhao, J.L. Liu, W.P. Beyermann, High-mobility Sb-doped p-type ZnO by molecular-beam epitaxy, Appl Phys Lett. 87 (2005) 152101. https://doi.org/10.1063/1.2089183.

[140] X. Pan, Z. Ye, J. Li, X. Gu, Y. Zeng, H. He, L. Zhu, Y. Che, Fabrication of Sb-doped p-type ZnO thin films by pulsed laser deposition, Appl Surf Sci. 253 (2007) 5067–5069. https://doi.org/10.1016/j.apsusc.2006.11.014.

[141] J. Ayres de Campos, T. Viseu, A.G. Rolo, N.P. Barradas, E. Alves, T. de Lacerda-Arôso, M.F. Cerqueira, Electrical and Raman Scattering Studies of ZnO:P and ZnO:Sb Thin Films, J Nanosci Nanotechnol. 10 (2010) 2620–2623. https://doi.org/10.1166/jnn.2010.1381.

[142] N. Sadananda Kumar, K. v. Bangera, G.K. Shivakumar, Properties of antimony doped ZnO thin films deposited by spray pyrolysis technique, Semiconductors. 49 (2015) 899–904. https://doi.org/10.1134/S1063782615070143.

[143] G. Li, X. Lin, S. Liu, B. Jia, Q. Wang, Sb content dependent thermoelectric properties of the p-type ZnO:Sb films fabricated by oxidation method, Appl Surf Sci. 439 (2018) 82–87. https://doi.org/10.1016/j.apsusc.2018.01.068.

[144] N. Fathima, N. Pradeep, J. Balakrishnan, Investigations of the effects of electrode geometry and mechanical stress on Antimony doped Zinc Oxide nanostructures based MSM UV photodetectors fabricated on flexible substrates, Solar Energy Materials and Solar Cells. 194 (2019) 207–214. https://doi.org/10.1016/j.solmat.2019.02.016.

[145] A.T.T. Pham, O.K.T. Le, T.T.T. Phan, D. van Hoang, T.H. Nguyen, N.D. Le, T.B. Phan, V.C. Tran, Enhancing transparent thermoelectric properties of Sb-doped ZnO thin films via controlled deposition temperature, Vacuum. 202 (2022) 111137. https://doi.org/10.1016/j.vacuum.2022.111137.

[146] J.M. Ribeiro, F.J. Rodrigues, F.C. Correia, I. Pudza, A. Kuzmin, A. Kalinko, E. Welter, N.P. Barradas, E. Alves, A.P. LaGrow, O. Bondarchuk, A. Welle, A. Telfah, C.J. Tavares, The influence of Sb doping on the local structure and disorder in thermoelectric ZnO:Sb thin films, J Alloys Compd. 939 (2023) 168751. https://doi.org/10.1016/j.jallcom.2023.168751.

[147] E.H. Hall, On a New Action of the Magnet on Electric Currents, American Journal of Mathematics. 2 (1879) 287. https://doi.org/10.2307/2369245.

[148] Hall effect | Definition & Facts | Britannica, (n.d.). https://www.britannica.com/science/Hall-effect (accessed January 19, 2023).

[149] J. Sánchez-González, A. Díaz-Parralejo, A.L. Ortiz, F. Guiberteau, Determination of optical properties in nanostructured thin films using the Swanepoel method, Appl Surf Sci. 252 (2006) 6013–6017. https://doi.org/10.1016/j.apsusc.2005.11.009.

[150] J. Martin, W. Wong-Ng, M.L. Green, Seebeck Coefficient Metrology: Do Contemporary Protocols Measure Up?, J Electron Mater. 44 (2015) 1998–2006. https://doi.org/10.1007/s11664-015-3640-9.

[151] SEMAT, (n.d.). http://www.semat.lab.uminho.pt/Equipamento.htm (accessed January 20, 2023).

APPENDIX

A. DEPOSITION SCHEMATICS

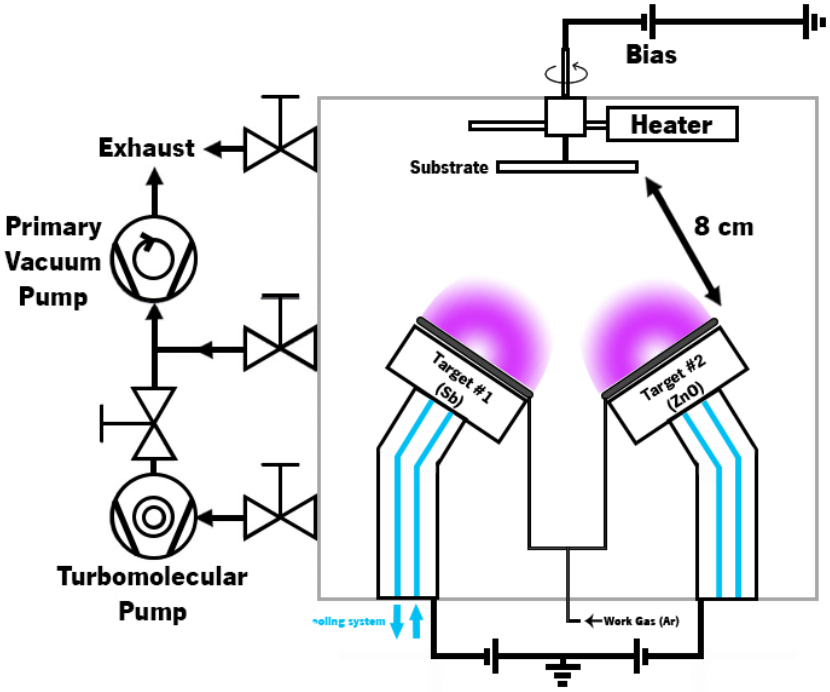

Figure A.1: Schematic of the sputtering deposition chamber.

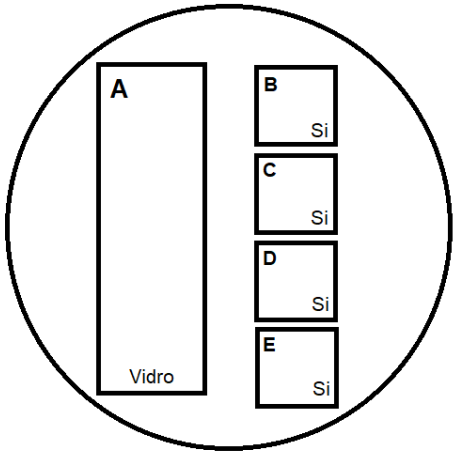

Figure A.2: Layout of the substrate holder.

B. RELEVANT PROPERTIES AND IMAGES

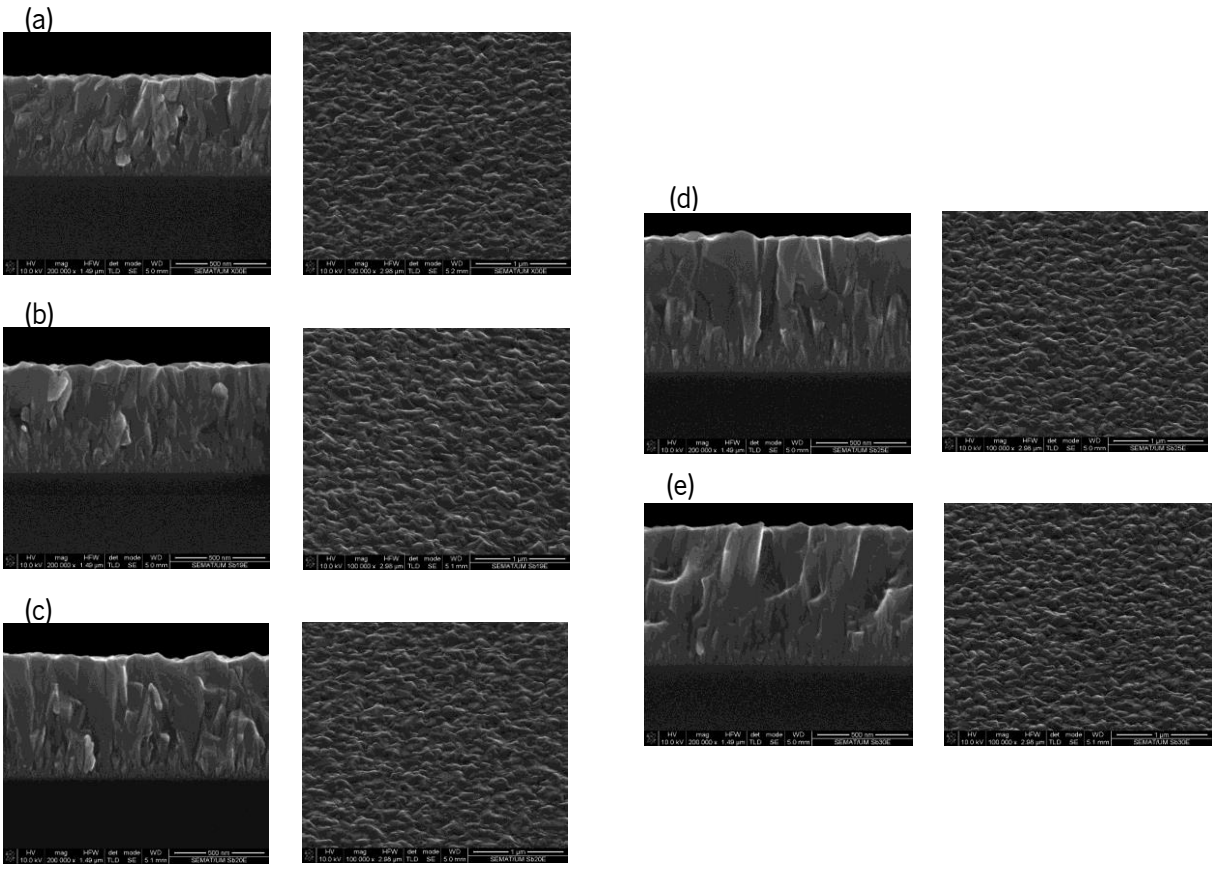

Figure B.1: : SEM images of the cross-section and surface of the (a) ZnoX, (b) ZnOSb:00, (c) ZnO:Sb01, (d) ZnO:Sb11 and (e) ZnO:Sb21 samples.

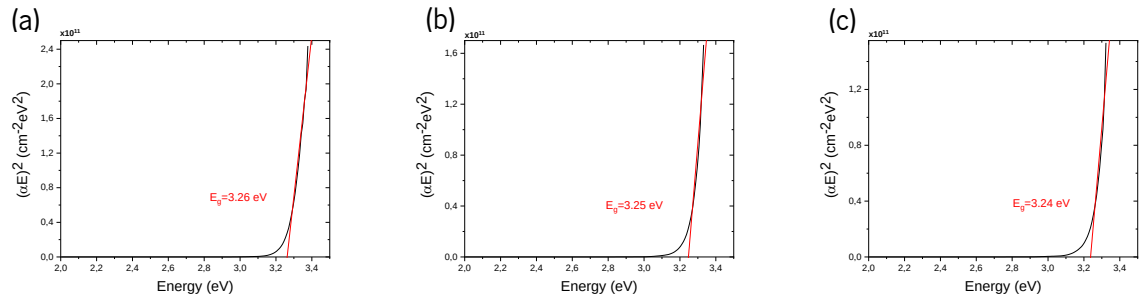

Figure B.2: Examples of Tauc plot calculated with *Dcalc* for sample (a) ZnO:Sb00, (b) ZnO:Sb11 e (c) ZnO:Sb21.

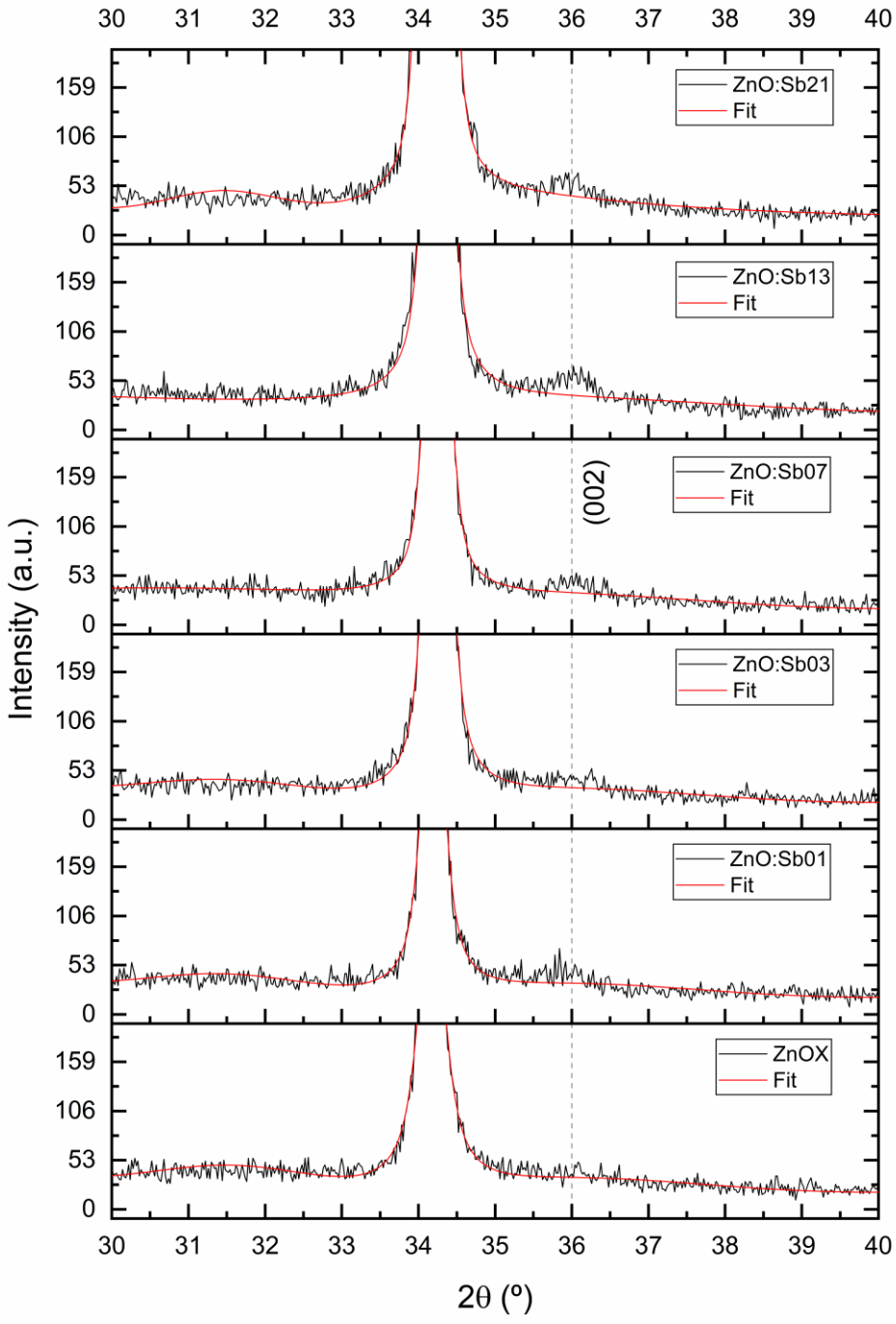

Figure B.3: Zoomed in XRD patterns for ZnOX, ZnO:Sb01, ZnO:Sb03, ZnO:Sb07, ZnO:Sb13 and ZnO:Sb21, to highlight the small peak at around 36°, that belongs to the (002) plane of Sb, which was not visible in the other graphic with the full XRD pattern.

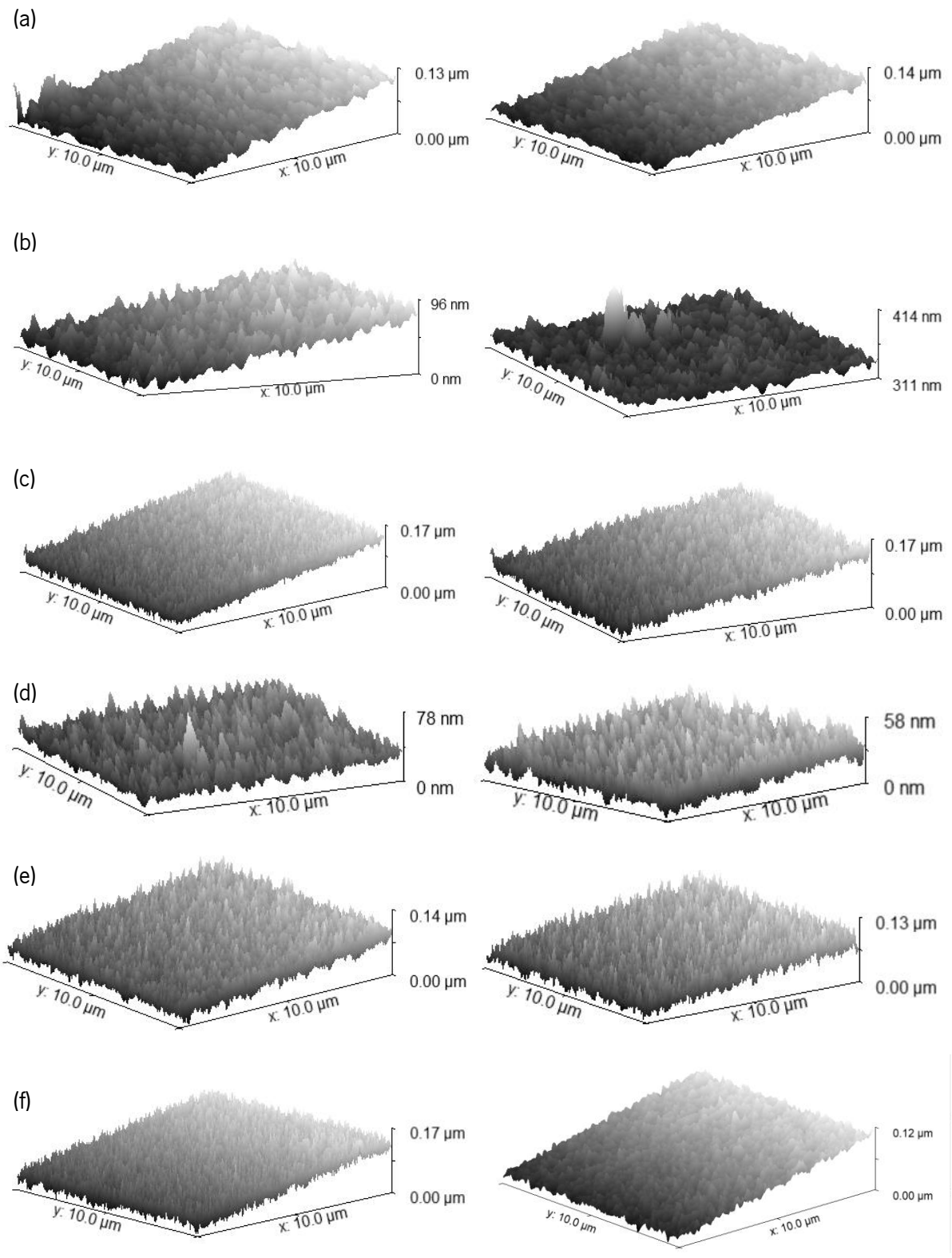

Figure B.4: AFM images of (a) ZnOX, (b) ZnO:Sb01, (c) ZnO:Sb03, (d) ZnO:Sb07, (e) ZnO:Sb13 and (f) ZnO:Sb21 thin films.